Fabrication and characterization of a novel mullite-stainless steel composed hollow fibre membrane for oil/water separation

Najib Meftah Almukhtar Omar [a,b], Mohd Hafiz Dzarfan Othman [a,*], Zhong Sheng Tai [a], Juhana Jaafar [a], Mukhlis A Rahman [a], Mohd Hafiz Puteh [c], Suriani Abu Bakar [d], Tonni Agustiono Kurniawan [e], Tao Li [f]

[a] Advanced Membrane Technology Research Centre (AMTEC), Faculty of Chemical and Energy Engineering (FCEE), Universiti Teknologi Malaysia, 81310 UTM, Skudai, Johor, Malaysia
[b] Chemical Engineering Department, Sabratha Faculty of Engineering, Sabratha University, Libya
[c] Faculty of Civil Engineering, Universiti Teknologi Malaysia, 81310 Skudai, Johor, Malaysia
[d] Nanotechnology Research Centre, Faculty of Science and Mathematics, Universiti Pendidikan Sultan Idris, 35900 Tanjung Malim, Perak, Malaysia
[e] College of the Environment and Ecology, Xiamen University, Xiamen 361102, Fujian, China
[f] School of Energy & Environment, Southeast University, Nanjing 210096, China

ARTICLE INFO

ABSTRACT

Low-cost mullite-kaolinite material has recently received more attention as an alternative to conventional ceramic materials such as alumina and silica to prepare ceramic hollow fibre membranes (CHFMs) due to its high alumina contents and silica and thermal/chemical stability. However, weak bending strength is still one of the key bottlenecks that delay their commercial applications. In this work, we successfully fabricate a novel mullite-SS HFM with enhanced bending strength using mullite-kaolinite power with different stainless steel alloy (SS) 316 L contents of 0.0, 2.5, 5.0, 7.5, 10 and 12 % (w/w) as a reinforcement material by phase inversion/sintering techniques. The SS alloy was a potential material to enhance the mechanical strength of mullite HFMs due to its excellent mechanical properties. The effects of the major fabrication parameters of SS contents, mullite contents, and fabrication parameters such as air gap distance and bore fluid flow rates were well studied and evaluated through the fabrication process. Fabricated mullite-SS HFMs were characterized by morphology, porosity, pore size/pore size distribution, and bending strength. Afterwards, they were evaluated in an oil/water separation system regarding water flux and oil rejection rate. Based on the findings, there was a gradual increase in the bending strength from 32.1 to 79.8 MPa with increased SS contents from 0 to 12 % (w/w). At 10 % (w/w) SS, the satisfactory morphology with the balance between the bending strength of 66.7 MPa and porosity of 29 % was obtained. This bending strength was significantly higher than reported for mullite-kaolinite HFMs in previous works. Moreover, At 10 % (w/w) SS, the oil–water rejection performance of 96.9% and the water permeation of 290 L/m². h was satisfactory at the sintering temperature of 1300 °C. These findings suggest the advantage of this membrane for various water treatment applications, such as oil/water separation, due to its outstanding physical properties.

1. Introduction

Water pollution is one of the significant global challenges nowadays. It has been growing continually due to the high water consumption by the increasing population and because of a variety of industrial applications worldwide [1]. Developing techniques for treating water has recently received popularity since water pollution seriously brings long-term impacts on public health and the environment [2]. Various treatment technologies have been developed and tested to address the global problem for feasibility and applicability [3]. Due to its adaptability, simplicity of use, energy-efficient and cost-effectiveness, membrane separation technology represents one of the most promising water treatment techniques [3,4]. The technique is widely known for effectively handling oil/water separation because of its cost-effectiveness and excellent oil removal performance [5,6]. Ceramic membranes have an enormous industrial possibility for effective oil/water separation due to their outstanding chemical and physical stability, reducing operation costs [7]. Lahiere and Goodboy [8] reported the first use of ceramic membranes for oil/water separation. They used a tubular

* Corresponding author.
E-mail address: hafiz@petroleum.utm.my (M.H.D. Othman).

ceramic membrane fabricated from alumina and tested it for oil/water separation in a U.S. petrochemical plant. The separation performance of the membrane reached about 94%, with a water permeation of 12.26 m^3/day.

Ceramic hollow fibre membranes (CHFMs) have recently gained more popularity in separation/filtration applications due to their higher surface area-to-volume ratio, compactness, and effective performance compared to other ceramic membrane modules [4]. Most of the previous works on CHFMs have been dedicated to the preparation of CHFMs of alternative nature, low-cost materials using mullite-based kaolinite [5], bauxite [9], industrial fly ash wastes [10], alumina-mullite [11], rice husk ash [12], and mullite-based ball clay [13] with microporous structure and attempt for a high porosity to improve the water permeation.

To do common things uncommonly, researchers have recently paid attention to fabricating CHFMs from low-cost mullite materials due to their superior properties compared to other low-cost materials [14]. Mullite can be a proper alternative to conventional ceramic materials such as alumina and silica to prepare CHFMs due to its high aluminosilicate content, high thermal resistance, low thermal expansion/conductivity and high chemical and mechanical stability [4,14]. According to the literature, mullite powder can be prepared chemically using different materials such as bauxite [9], ball clay [13], kaolin clay [15] and kaolinite [5]. Among all the materials, kaolinite showed better physical properties, such as high mechanical properties, high refractory properties and low plasticity. However, the CHFMs fabricated by kaolinite powder as a low-cost material typically show a low bending strength of 14 MPa at a sintering temperature of 1350 °C due to the low density of kaolinite of 2.4 g/cm^3 [4,5]. To overcome this bottleneck, several studies have increased the mechanical properties of the kaolinite-based HFMs by transforming kaolinite into mullite through a series of chemical reactions with a higher density of 3.11–3.26 g/cm^3 [4,14]. For example, Twibi, et al. [5] fabricated the initial mullite-kaolinite HFMs with a higher mechanical strength of 86 MPa than kaolinite HFM.

Despite their technological strength, mullite-based HFMs are brittle and have weak bending strength due to their microstructure pores, thin walls, weak bonds, and the nature of ceramic material, which is fragile [5]. According to Schmeda-Lopez, et al. [16] and Duke, et al. [17], the brittleness of CHFMs increases their breaking dangers at high operational conditions, including pressures, flow rates, and vibration, as well as the supports of CHFMs, tend to collapse at the membrane interface and seals [4]. This constrains their commercialization in practical industrial applications and affects their filtration performance.

To cope with this bottleneck, several studies reported that adding reinforcement materials was deemed feasible to enhance the bending strength of CHFMs fabricated from low-cost materials and open the path for CHFMs to be commercially applied in water treatment applications for long operations. Several studies on CHFMs fabrication employed reinforcement materials, such as vanadium pentoxide (V_2O_5) [18], vanadium attapulgite clay [19], and yttrium oxide (Y_2O_3) [20], to improve the bending strength of low-cost CHFMs for various water treatment applications. However, all these reinforced CHFMs still exhibit weak bending strength.

Although superior properties of stainless steel alloy (SS) 316 L include high corrosion resistance, high corrosion resistance, high resistance to chemicals and chlorides due to its nickel and molybdenum content, high-temperature resistance, high mechanical strength, and excellent robustness [21], to the best of our knowledge, no previous study has incorporated SS as a reinforcement material to enhance the bending strength of mullite HFMs. To bridge this knowledge gap, this work develops the bending strength of mullite HFMs using different strengthening SS contents (i.e., 0, 2.5, 5.0, 7.5, 10 and 12% (w/w)) as a strengthening material by phase inversion/sintering technique for effective oil/water separation.

The primary role of using the SS powder was to fill the large gaps between the mullite particles to reinforce the bending strength of the prepared membranes, stabilizing the structure of pores, and reducing the large pores sizes of the mullite-kaolinite HFM. Before the membrane preparation, the mullite and SS powders were characterized by X-ray fluorescence (XRF), X-ray diffraction (XRD) and Brunauer–Emmett–Teller (BET) method. Subsequently, the mullite-SS HFMs were characterized in terms of the effect of the fabrication parameters, such as SS contents, air gap distance, and bore fluid flow rate on the physical properties of mullite-SS HFMs, including morphology, bending strength, pore size, porosity, pore size distribution to obtain the best SS content that provides the best physical properties to fabricate mullite-SS HFMs. In addition, the performance of oil–water separation of mullite-SS HFMs concerning oil rejection rate and water flux was further evaluated and compared to those of previous studies.

2. Materials and methodology

2.1. Materials

Mullite-kaolinite powder with a particle size of 18 μm was purchased from Shijiazhuang Huabang Mineral Co., Ltd Chania and used as a primary ceramic material. SS alloy powder (SS 316L) with a particle size of 3 μm was obtained from Alfa Aesar and used as reinforcement material. N-methyl-2-pyrrolidone (NMP) was supplied by Sinopharm Chemical Reagent Co., Ltd. and used as a solvent. Arlacel (P135, CRODA) was used as a dispersant. Polyethersulfone (PESf, Radel A-300, Ameco Performance) was purchased from Amoco Chemicals and used as a polymer binder and a viscosity enhancer. Distilled and tap water were used as internal and external coagulants, respectively. Mullite powder, SS 316L powder, and PESf were dried at 60 °C before use, and NMP was used without further treatment.

2.2. Material characterizations

Characterization of mullite/SS powders played an important role in the integration quality between mullite/SS particles. Mullite/SS characterization provided a better understanding of the powder's composition, crystallinity, surface area etc. It also explained whether the alumina/silica contents in mullite powder, SS contents and their impurities met the required specifications. Therefore, fluorescence (XRF, Rigaku, Smart Lab, Japan) was applied to determine the composition of the mullite and SS powders at temperatures of 18 °C − 28 °C and relative humidity lower than 75%. First, mullite powder composition was obtained by combining 8 g of mullite powder with 2 g of cellulose wax which served as a binder to form a mixture of mullite and cellulose. Next, the mixture was pressed to 20–30 torr (mmHg) pressure to form a pellet, which was then placed in a sample holder for analysis.

X-ray diffraction (XRD, Rigaku, Smart Lab, Japan) analysis analyzed the crystalline structure of mullite and SS powders separately under ambient conditions. The examination was conducted by a Rigaku Smartlab X-ray diffractometer (Model: D5000 Siemens, Japan) with a copper anode. The sample was placed on a silica glass sample holder for spitting with a thin gold coating layer for 3 min under a vacuum. The diffraction patterns were generated by beta-filtered CuKα radiation with a wavelength (λ) of 1.5406 °A at 30 mA, and a 40 kV monochromator produced from a Pan Analytic Diffraction X-ray tube. The diffraction patterns were obtained

across a diffraction angle range of 10° to 80° with a step size of 0.026°, step time of 50 s, and a constant anti-scatter slit of 1/4.

The surface area of mullite and SS powders was evaluated by measuring the ability of mullite and SS powder to adsorption/desorption nitrogen at 196 °C. This method uses a micromeritics device with a high-resolution surface area analyzer (Model, Belsorp Max, BEL Japan Inc., Osaka, Japan) to measure the surface area of mullite and SS powder in relative pressures ranging from 0 to 0.99, whereas the specific surface area of BET was determined at classic relative pressures ranging from 0.05 to 0.30.

The thermogravimetry analysis (TGA) was used to evaluate the weight change of mullite and SS powders as a function of temperature using a TGA (Mettler Toledo, SDTA851^e). This analysis is important for determining the thermal stability and composition of mullite and SS powders. The TGA (Mettler Toledo, SDTA851e) conducted the thermal analysis. The samples were subjected to gradual heating from 30 to 1350 °C at a rate of 10 °C/min under a nitrogen (N$_2$) atmosphere. The degree of dihydroxylation, which indicates the loss of structural water, was determined through the following Equation (1) [22]:

Table 1
Composition of mullite and SS dopes suspension.

Dope suspension No.	Mullite (wt. %)	SS (wt. %)	Dispersant (Arlacel P135, wt. %)	NMP (wt. %)	PESf (wt. %)
1	57.0	0.0	1	35	5
2	54.5	2.5	1	35	5
3	52.0	5.0	1	35	5
4	49.5	7.5	1	35	5
5	47.0	10	1	35	5
6	45.0	12	1	35	5

$$D = 1 - \frac{(M_m - M_t)}{(M_m)} \tag{1}$$

where D: Degree of dihydroxylation, Mm: Maximum loss of mass, M_t: Loss of mass at a certain temperature in the TGA curve.
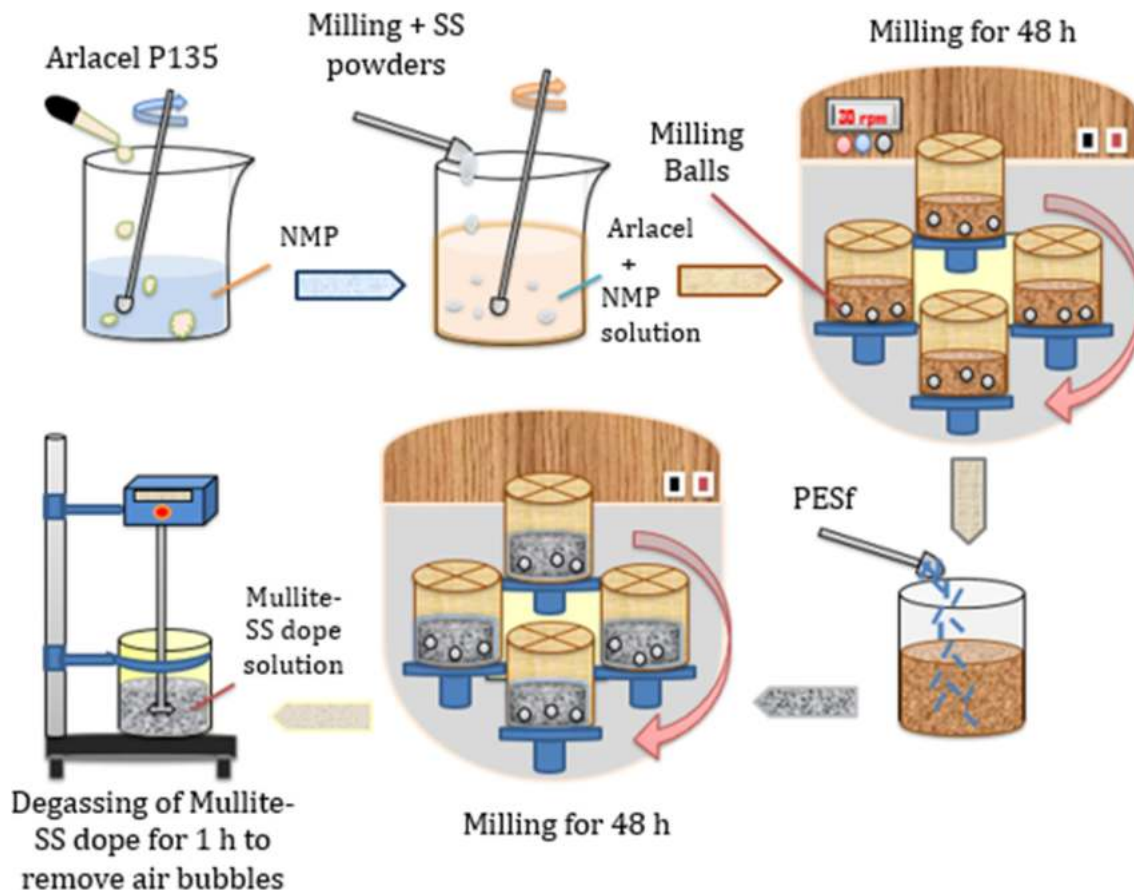
2.3. Fabrication of mullite-SS composed HFMs

The optimum ceramic loading in the dope suspension for ceramic membrane fabrication was 50–60% (w/w), as Li [23] reported earlier. Consequently, this study obtained the best continuous and stable resultant mullite HF at 57% loading and mullite-SS HFs ranging from 54.5 to 45.0 % loading. Based on this observation, five dope suspensions were prepared with different mullite and SS powder contents with a total solid loading of 57%, as presented in Table 1.

The Arlacel P135 dispersant was gently mixed in the NMP solvent until entirely dissolved. Arlacel (P135) is the most common dispersant for ceramic dope suspension preparation. This dispersant showed outstanding results in ceramic dope suspension preparation, as recorded in many studies in the literature [5,6,12,24,25]. The advantages of the Arlacel P135 are its function in improving the homogeneity and stability of the ceramic suspension, better control over the size and distribution of the ceramic particles in the suspension, reducing the accumulation/sedimentation of the ceramic particles and the ability to improve the adhesion between the particles of ceramic [26]. Afterwards, the mullite and SS powders mixture were batch-wise added to the NMP and Arlacel P135 mixture with gentle mixing in a milling jar. The mixture was milled for 48 h in a ball miller at 190 rpm to form a mullite-SS homogeneous dope suspension. Afterwards,

Fig. 1. Schematic diagram of mullite-SS dope suspension preparation steps.

the polymer binder (PESf) was added to the mullite-SS homogeneous dope suspension and subjected to a further 48 h milling using a ball miller at 190 rpm to attain homogenous dispersion of mullite and SS particles. Later, the mullite and SS dop suspension was degassed by gently mixing for 1 h at ambient temperature to remove trapped air in the dope suspension before spinning. The mullite and SS dope suspension separation steps are shown in Fig. 1. After degassing, the mullite-SS dope suspension was drawn into a SS syringe for extrusion and phase inversion. Next, the mullite-SS dope suspension and internal coagulant (distilled water) were spun together through a tube-in-orifice spinneret with an inner diameter of 1 mm and an external diameter of 2 mm by syringe pumps at a steady flow and ambient temperature to form mullite-SS HF pristine before immersing into the external coagulant bath (water bath). The spinning parameters are listed in Table 2.

Then, the mullite-SS HF precursor was kept in the water bath overnight to complete the phase inversion of the mullite-SS HF and NMP traces removal. Later, the mullite-SS HF precursors were dried overnight at ambient temperature and then cut 20 cm before passing to the sintering process. A schematic diagram of the extrusion of mullite-SS dope suspension and phase inversion technique is shown in Fig. 2.

The last stage was sintering the precursor mullite-SS HFs at 1350 °C based on the heating profile shown in Fig. 3. The sintering temperature profile for ceramic membranes can vary depending on the specific ceramic material and the desired properties of the final membrane. First, the furnace temperature increased from room temperature to 600 °C at a heat rate of 2 °C/min. Next, the temperature was fixed at 600 °C for 2 h to remove polymer binders to prevent defects and impurities during high sintering temperatures. Afterwards, the temperature was raised to reach the target temperature of 1350 °C and fixed for 6 h to sinter the mullite-SS HF precursor and form mullite-SS HFMs. At 1350 °C sintering temperature, proper solidification and integration between mullite and SS particles were obtained. In addition, at sintering temperatures below 1350 °C, the mullite-SS HFM was still brittle.

The final step was the reduction process of all fabricated mullite-SS HFMs fabricated at different SS contents using hydrogen (H_2) flow in a tubular furnace at 800 °C for 4 h to reduce any iron oxide (Fe_2O_3) formed to iron (Fe). This technique was preferable for the reduction process by H_2 to flowing H_2 during the sintering process of the mullite-SS HFMs for several reasons: 1) safety, 2) lower temperature used up to 800 °C, as compared to at sintering process, which reached 1350 °C, 3) less reduction of Fe_2O_3 to Fe was obtained. According to Rui, et al. [27], pure H_2 efficiently reduced the Fe_2O_3 to Fe up to 100%.

2.4. Characterizations of mullite-SS composed HFMs

The rheology behaviours of mullite and SS dope suspension were tested by Brookfield viscometer at a shear rate from 1 to 10 s^{-1}. Scanning Electron Microscopy (SEM, Hitachi Model TM 3000) was applied to characterize the morphology of prepared mullite-SS composed HFM at 30 kV and different magnifications. The sample was carefully snapped and located on a rectangular SEM stub and sputter-coated with a thin gold layer for 2 min under a vacuum before the analysis. The Instron tester (Model of 5544) was used for a three-point test to evaluate the bending strength
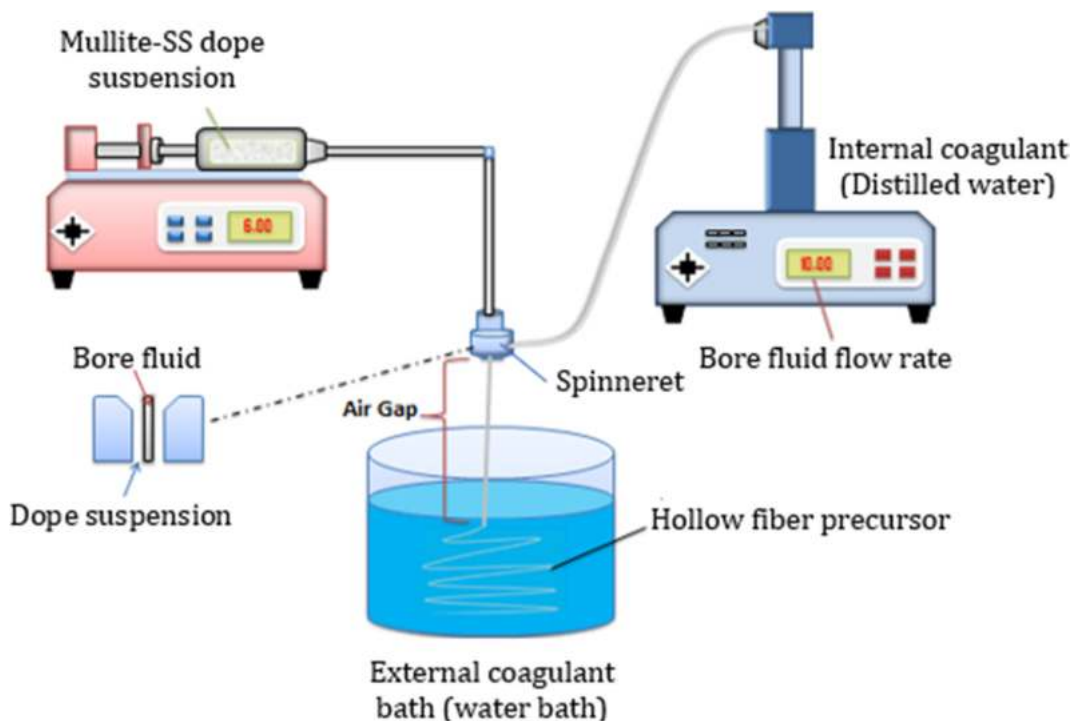
Table 2
Spinning parameters of mullite-SS HFs pristine.

Spinning parameters	
Air gap distance (cm)	5, 10, 15, 20
Bore fluid flow rate (ml/min)	4, 6, 8, 10
Extrusion rate (ml/min)	10
Extrusion pressure (bar)	1
Internal diameter of spinneret (mm)	1
External diameter of spinneret (mm)	2
Internal coagulant	Distilled water
External coagulant	Tap water

Fig. 2. Schematic diagram for extrusion and phase inversion technique.

of the mullite-SS HFM. The used load cell for this tensile tester was 1 kN. Next, the mullite-SS HFM was placed on a sample holder at a distance of 5 cm, and the speed loading applied on the sample was 0.25 mm/min till the membrane cracking occurred. The following Equation was used to estimate the bending strength of mullite-SS HFM [28]:

$$\sigma_F = \frac{8FLDo}{\pi \left(D_{o-}^4 D_i^4 \right)} \tag{2}$$

where σ_F (MPa): Bending strength, F (N): Load at the break, L (5 cm): Span length, D_o (m): Outer diameter and D_i (m): Inner diameter.

Mercury intrusion porosimetry (MIP, Micromeritics AutoPore IV 9500 Series, USA) was used to estimate the porosity, pore size, and pore size distribution of mullite-SS composed HFM. First, the sample was prepared by gently crashing the mullite-SS composed HFM into tiny pieces on a 5 cc penetrometer sample holder. Next, the measurement was gathered by mercury porosimetry at low pressure ranging from 38.6×10^3 to 4.2×10^3 bar to assure adequate mercury penetration into membrane pores. Then, the penetrometer was filled with mercury according to a low-pressure gauge. Next, the penetrometer was weighed and placed into the high-pressure orifice filled with the membrane sample and mercury. Finally, the porosity and the pore size were calculated, while the pore size distribution was graphed.

The hydrophilicity of the mullite-SS composed HFM was evaluated by measurement of contact angle value using the goniometer test (Model: OCA 15 EC, Dataphysics, Germany). The distilled liquid water drops were vertically dropped out on the different areas of the outer surface of the membrane. A high-resolution camera was used to monitor the change in the images. The average contact angle values were obtained to reduce the inaccuracy throughout the test. This test was repeated more than 3 times to obtain a more accurate result. The crossflow filtration system was used to evaluate the water permeation and oil rejection efficiency of membranes, as shown in Fig. 4. The test was carried out at a pressure of 2 bar for 120 min. The water permeation was determined by collecting the penetrable volume in unit time and area as described by the following Equation.

$$J = \frac{V}{A \times \Delta t} \tag{3}$$

where: J (L/h.m^2): flux, V (L): collected water volume on the permeate side, Δt (10 min): collecting time of water, and A (m^2): membrane area.

2.5. Oil rejection performance measurement

The performance of mullite-SS HFMs for oil rejection from the water was evaluated using three different oil/water emulations with varying concentrations of vegetable oil (i.e. 1000, 1500, and 2000 ppm). To prepare the oil–water emulsion samples with con-
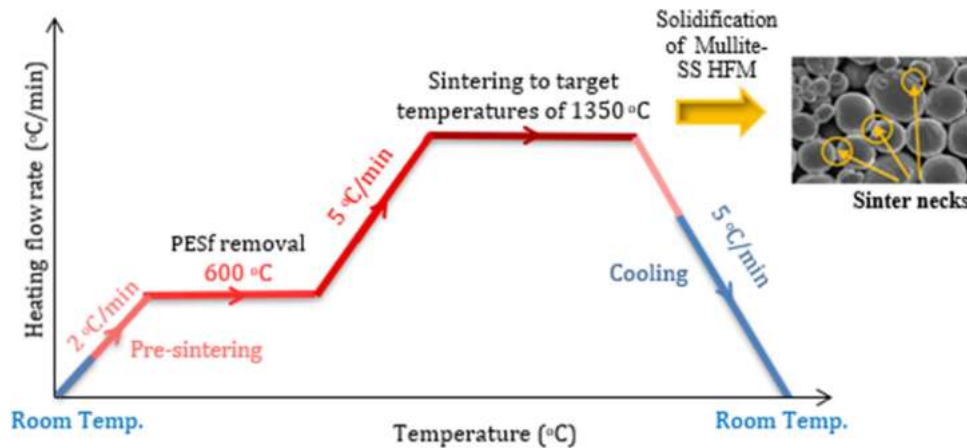

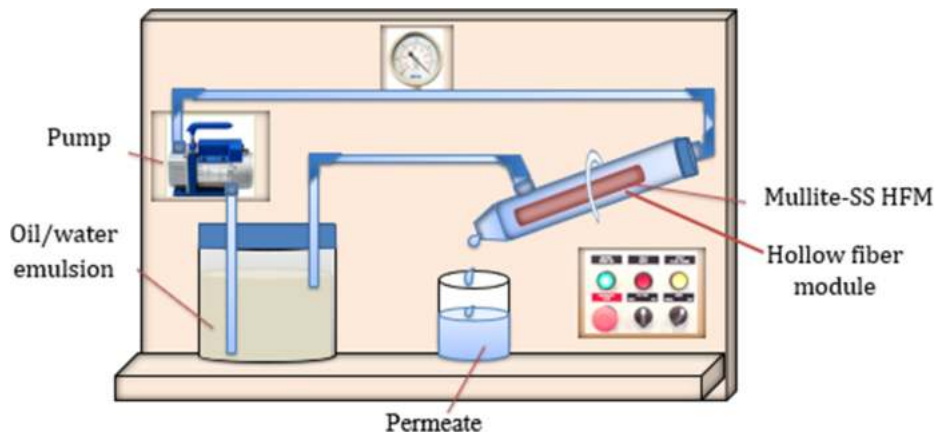**Fig. 3.** The sintering temperature profile of mullite-SS HF precursor.

Fig. 4. Schematic diagram of the oil/water filtration system.

centration1000, 1500, and 2000 ppm at room temperature, 2, 3 and 4 g of oil were added to 2 L of distilled water. Sodium dodecyl sulfate (an anionic surfactant) was also added to each oil–water emulation in a 1:4 ratio [28]. A mixer homogenizer (Model: EKOMIX 2403, China) was used to stir the mixture at 1200 rpm for 20 min until the SDS fully dissolved, resulting in a homogenous oil–water emulsion. The non-appearance of an oil layer confirmed the stability of the produced oil–water emulsion at the surface after 4 days and no other indications of degradation related to coalescence or loss of homogeneity. A crossflow microfiltration system was used for this test for 120 min. The membrane module used in this study comprised a cylindrical stainless steel housing including three mullite-SS HFMs with an active length of 10 cm. The oil–water emulsion was pumped from a 4 L feed tank using a centrifugal pump. The flow velocity and pressure were measured using a flow meter and two manometers, respectively, and were set to 1.5 bar and 2.0 L/min, respectively. The filtered water was collected in a clean container positioned underneath the end of the membrane module. Before and after filtration, the oil/water feed absorbance levels were measured using a visible spectrophotometer (UV, DR500, Hach) at a wavelength of 273 nm. The rate of oil rejection was calculated using Equation (4).

$$R = \frac{C_f - C_p}{C_f} \times 100\% \tag{4}$$

where R (%): Oil rejection, C_f (g/L): Concentration of the feed and C_p (g/L): Concentration of permeate.

Table 3
Mullite-kaolinite and SS chemical composition analysis.

| Components	Mullite-kaolinite % (w/w)	SS % (w/w)
SiO_2	59.6	–
Al_2O_3	39.1	–
Fe_2O_3	0.5	–
TiO_2	0.7	–
Cr	–	18.0
Ni	–	10.0
Fe	–	69.0
Mo	–	3.0

3. Results and discussion

3.1. Properties of mullite and SS powders

The chemical compositions of mullite and SS powders were determined via XRF analysis, as indicated in Table 3. Mullite was mainly composed of silica and alumina, with respective contents of 59.6 and 39.1 % (w/w). Interestingly, the total alumina and silica content of mullite (98.7 % (w/w)) were higher than other alternative ceramic materials, such as palm oil fuel ash [29], waste sugarcane bagasse ash [30], zeolite [31], corn cab ash [32], and bentonite [28].

According to the XRD curve in Fig. 5 (A), mullite and quartz were the dominant crystalline phases in the mullite sample. The mullite sample also contained minor cristobalite phases. Meanwhile, the XRF results show that SS powder was composed of iron (Fe) (69% w/w), chromium (Cr) (18 % (w/w)), nickel (Ni) (10 % (w/w)) and molybdenum (Mo) (3% (w/w)). This result was consistent with the XRD results in Fig. 5 (B), demonstrating high Fe, Cr, and Ni intensity.

The BET hysteresis was used to evaluate the surface area of mullite and SS powders as a function of pore size/particle size. The hysteresis in this analysis was attributed to the thermodynamic effect, network effect or both. This analysis used capillary condensation and multilayer adsorption in mesoporous solids adsorption for VI and V isotherms types. As seen in Fig. 6 (A) and (B), the BET surface areas of mullite and SS were 23.4 and 1.5 m²/g, respectively. The reason for the tendency of mullite towards a higher surface area than SS could be attributed to the differences in particle size, aggregate distribution, porosity, and size distribution, especially for fine and small particles such as SS particles. Additionally, it could be attributed to the fact that large particles size, such as mullite particles, had a perfect shape, whereas very small microparticles, such as SS particles, behaved similarly to nanoparticles which usually did not have a regular/entire shape. Their size most likely was shown to be equivalent to sphere diameter. In other words, the volume of very small particles was measured first and then converted to a diameter of a sphere with the same particle volume [28 33]. The V isotherm type was produced corresponding to the IUPAC classification method, and the H1 isotherms loops type was observed for mullite and SS powders. According to Ayinla, et al. [34], the data portrays H1 isotherms usually describe materi-
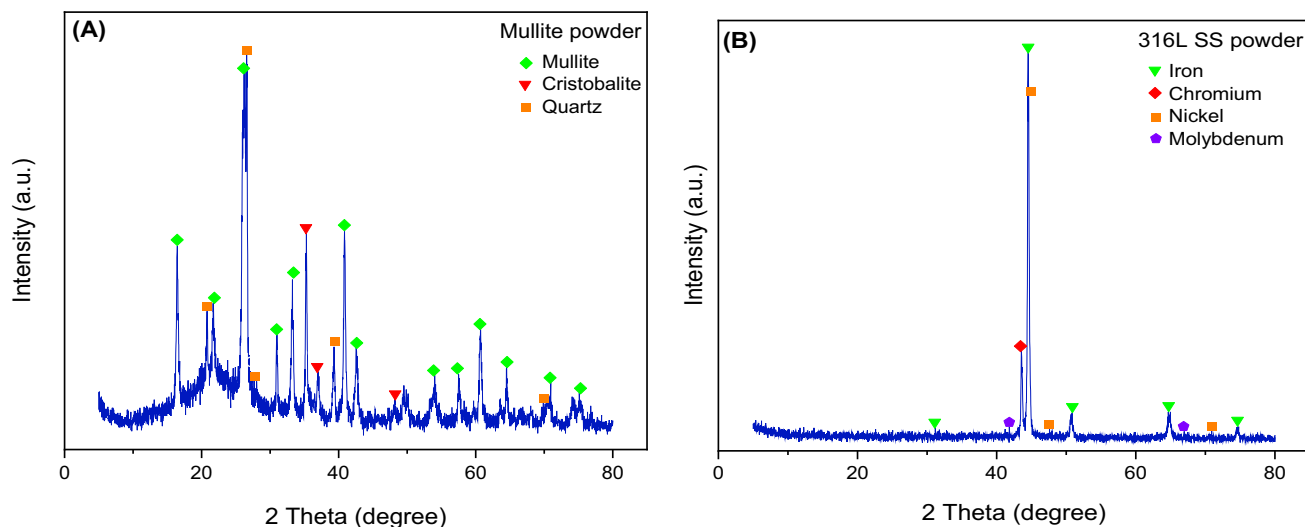
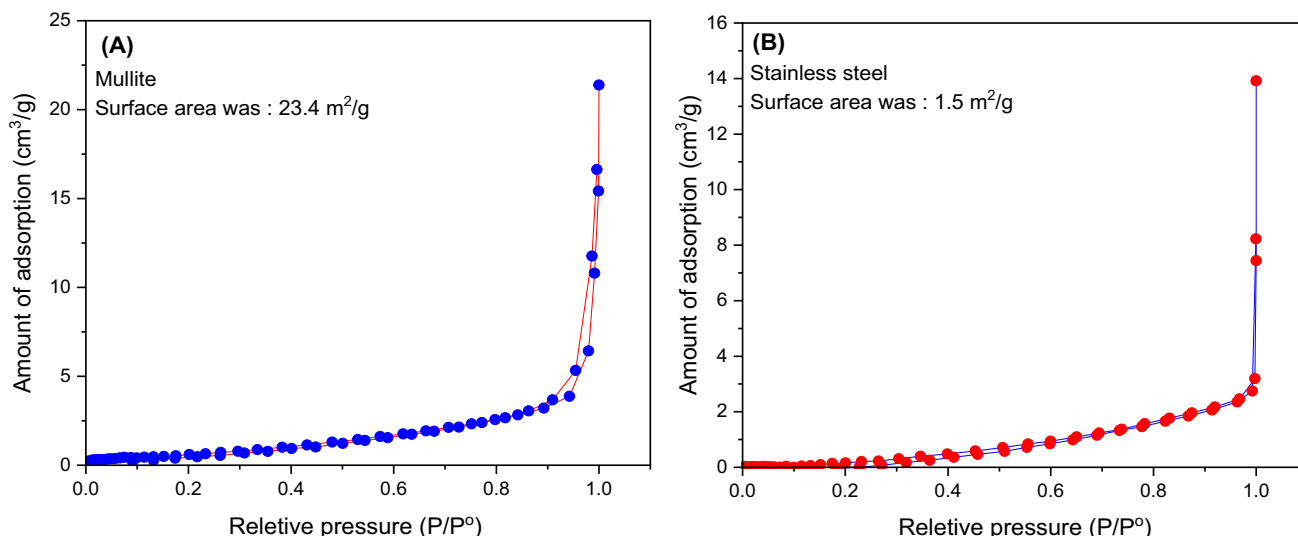**Fig. 5.** XRD pattern of (A) mullite powder and (B) SS powder.

Fig. 6. BET surface areas of mullite and SS powders.

als with narrow distribution and uniform cylinder-shaped pores and show a better consistent pore size and simple pore connection.

The thermogravimetry analysis (TGA) results for mullite-based kaolinite, and SS 316 L powders are shown in Fig. 7 (A & B) as curves representing the weight loss as a function of temperature presented in the sintering profile in Fig. 3. As seen in Fig. 3, in the pre-sintering step from room temperature of 31 °C to about 600 °C, the mullite powder displays a gradual weight loss of about 0.417%, as shown in the TGA curve (Fig. 7, A). This significant weight loss could be attributed to the loss of the hydroxyl (OH) group bonded to the water molecule and the decomposition of organic materials, as reported elsewhere in the literature [13]. Additionally, it could be attributed to the structural water loss from the mullite powder. However, increasing the temperature from room temperature to 600 °C (pre-sintering step) for SS 316 L increases the weight of SS gradually, as exhibited in the TGA curve in Fig. 7 (B). The reason for this could be the gradual release of the adsorbed gases by SS powder at low temperatures, which increases the SS weight [35].

Above 600 °C, the mullite weight increased (see Fig. 7, A). This increase could be because when the temperature is above 600 °C,

mullite undergoes a phase transformation and releases some SiO_2 as a gas. This results in weight loss in the mullite [36]. On the other hand, during this phase transformation, the Al2O3 molecules in the material react with the remaining SiO_2 to form a new mullite phase with a higher aluminium content. This phase has a higher density than the original mullite and contributes to the observed weight gain in the mullite [36]. As for SS, a sharp weight increase was observed over 600 °C, as shown in Fig. 7, B. This increment could be attributed to the quick oxidation of SS due to the presence of chromium, which forms a protective oxide layer on the surface of the steel [37]. At high temperatures, this oxide layer may start to break down, leading to the oxidation of the steel. The oxidation of steel results in the formation of metal oxide, which is heavier than the original steel [38]. This may also contribute to the weight increase observed during TGA analysis. The decomposition of organic compounds in the SS could also increase the SS weight at high temperatures. The decomposition of these compounds could release gases such as carbon dioxide or water vapour, which can contribute to the weight increase observed during TGA analysis. A similar trend of the TGA curve of SS 316 L was reported in the literature by Jang, et al. [37].
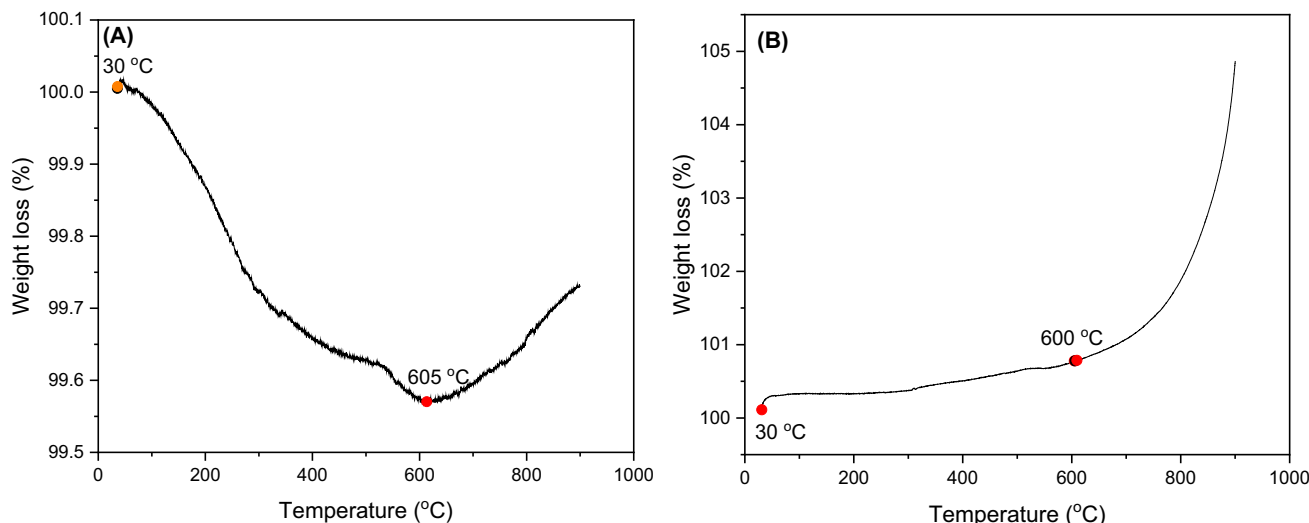

Fig. 7. Thermogravimetry analysis (TGA) of (A) mullite-kaolinite powder and (B) SS powder.

3.2. Rheological characteristics of dopes suspension

The effects of varying the SS contents (0.0, 2.5, 5.0, 7.5, 10 and 12 % (w/w)) on all mullite-SS dopes suspension viscosity were studied through shear rates between 1 and 10 s^{-1}. As seen in Fig. 8, the effects of the SS contents on the viscosity of all mullite-SS dopes suspensions differed. The dope suspension with 12% (w/w) SS showed the highest viscosity, while the suspension with the SS loading of 0 % (w/w) showed the lowest viscosity. The suspension viscosity obviously increased when the SS contents in the dope suspensions were increased from 2.5, 5.0, 7.5, 10 to 12 % (w/w). Several reasons could explain this observation, such as increased particle concentration, particle size, interparticle interactions, and surface charge changes. Adding SS to the mullite dope suspensions resulted in an increased concentration of suspended particles, which increased the viscosity of the dope suspensions. The increase in concentration caused the particles to become more closely packed, leaving less space for the fluid to flow through. This increased crowding creates greater internal friction, leading to higher viscosity. Adding SS to a mullite suspension also increased the size of the suspended particles. With an increased particle size, the viscosity of the suspension escalated due to the amplified contact area between particles, creating higher friction and resistance to flow. Ceramic particles generally possess a negative surface charge that hinders their tendency to aggregate by repelling each other. However, when SS was added to mullite dope suspensions, the surface charge of the particles changed, facilitating their attraction towards one another and leading to the formation of aggregates and increased viscosity of the dope suspensions. Furthermore, incorporating SS into a mullite dope suspension affected the interaction between the ceramic particles. Introducing SS particles to the mullite suspension formed the bonds between SS and mullite particles, resulting in a network of particles more resistant to flow. Consequently, this increases the viscosity of the dope suspensions. This finding was similar to that of Deng, et al. [39], who reported that a gradual increase in the titania (TiO_2) from 0 to 9 % (w/w) to the mullite dope suspension led to a gradual increase in the dope suspension viscosity.

Another significant observation was that all dope's suspension viscosities obeyed the shear rate pattern, where increasing the shear rate reduced the viscosity of all dope suspensions. This observation was similar to that reported in many studies for decreasing the dope solution's viscosity with increasing the share
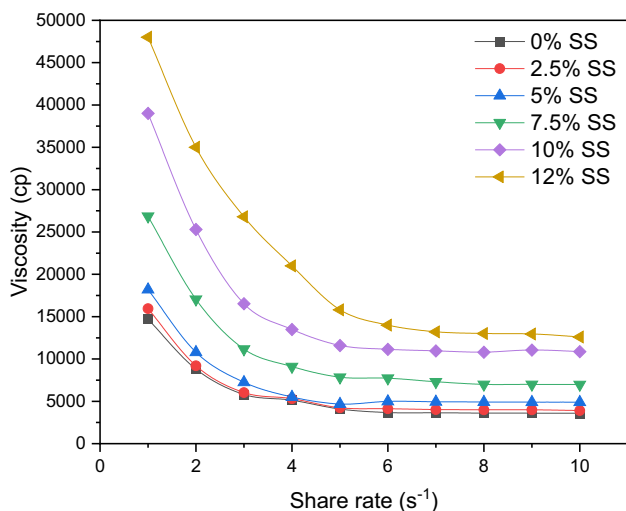
rate [40–42]. At shear rates from $1 - 4$ s^{-1}, the viscosity difference between all dope suspensions was obvious because the dopes had non-Newtonian flow behaviour and displayed shear-thinning features. In contrast, at shear rates behind 5 s^{-1}, no obvious viscosity difference was observed because the dopes behaved almost Newtonian flow.

3.3. Characteristics of mullite-SS HFMs

HFMs with different SS loadings ranging from 0 to 12 % (w/w) were successfully fabricated through the phase inversion/sintering technique. The total loading of mullite-kaolinite and SS was always maintained at 57 % (w/w) for all HFMs. Fig. 9 shows the photographic images of HFMs with different SS loadings. The HFM was white in colour when there was no SS loading. With increasing SS loadings from 2.5 to 7.5 % (w/w) SS, the HFMs turned greyish. The HFM with 10 and 12 % (w/w) SS became dark grey, attributed to the high content of SS that was dark grey.

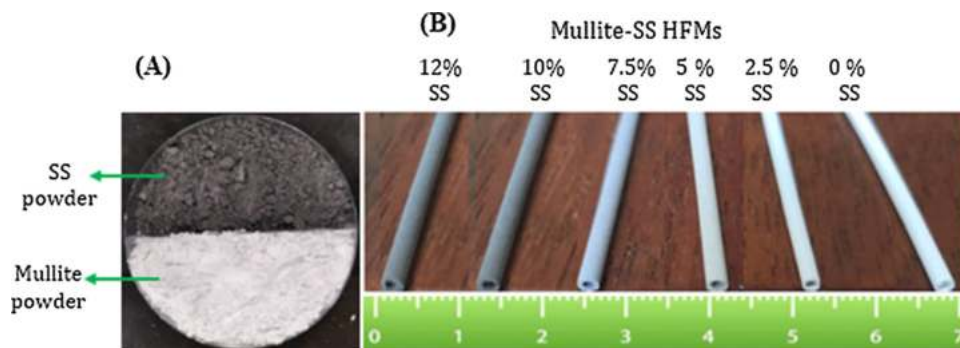### 3.3.1. Phase change of mullite-SS HFMs

The effects of different SS contents on porous mullite-SS HFMs phase composition were studied by XRD analysis, as shown in Fig. 10. The main crystal phase of all mullite-SS HFMs was the mullite with a minor cristobalite crystal phase. By adding the SS content to the mullite HFM, two more crystal peaks of iron oxide (Fe_2O_3) and nichrome appeared (Fig. 5). It was worth mentioning that nichrome had a silvery-grey colour and several outstanding properties that effectively improved the properties of the mullite-SS HFMs, such as high mechanical strength, electrical resistance, and oxidation resistance [43]. The gradual increase of SS contents in the mullite-SS HFMs further increased the peaks of the nichrome crystal phase and decreased the cristobalite and mullite crystal phases. As a result, the highest peaks of the nichrome crystal phase and the lowest cristobalite and mullite crystal phase were recorded in the mullite-SS HFM containing 12 % (w/w) SS.

In contrast, the highest cristobalite and mullite peaks were observed at the mullite HFM with 0.0 % (w/w) without nichrome peaks. Moreover, there were no notable changes in the intensity of the cristobalite and mullite peaks when the SS loading increased from 0 % (w/w) to 2.5 % (w/w), while the obvious increase was noted when the SS loading increased from 5.0 to 12 % (w/w). On the other hand, the peaks of cristobalite and mullite peaks in mullite SS HFM containing SS loading from 5.0 to 12 % (w/w) SS slightly decreased over the mullite SS HFMs with 0.0 and 2.5 % (w/w) SS.

As depicted in Fig. 10, the mullite-SS HFM with 45 % (w/w) mullite and 12 % (w/w) SS had the highest cristobalite/nichrome contents and the lowest mullite content, as compared to other mullite-SS HFMs containing mullite/SS of 47/10, 49.5/7.5, 52/5.0, 54.5/2.5 and 57/0.0. In contrast, the highest mullite content with the lowest cristobalite/nichrome contents was observed at mullite HFM with 0.0 % (w/w) SS and 57 % (w/w) mullite HFM. A gradual increase in cristobalite/nichrome contents was obtained with an increase in SS contents from 0.0, 2.5, 5.0, 7.5, 10 to 12 % (w/w) in the mullite-SS HFMs, while a gradual reduction in mullite content was observed with an increment in the SS contents from 0 to 10 % (w/w).

The XRD analysis was also conducted to evaluate the reduction of Fe_2O_3 in the composition of the mullite-SS HFMs sintered at 1350 °C to iron (Fe) form. The XRD pattern in Fig. 10 before the reduction reaction shows the Fe_2O_3 peaks at two theta degrees of 30.7°, 36.1°, 43.9°, 58.1°, 63.84° and 69.9°. After the reduction reaction of Fe_2O_3 was achieved using H_2 at 800 °C for 4 h, an obvious reduction was observed, and all Fe_2O_3 peaks successfully shifted to the Fe except one peak shifted from Fe_2O_3 to FeO at θ of 43.9°, as exhibited in the XRD pattern in Fig. 10 (after reduction). According to Rui, et al. [27], the oxidation of Fe_2O_3 and FeO could be fur-

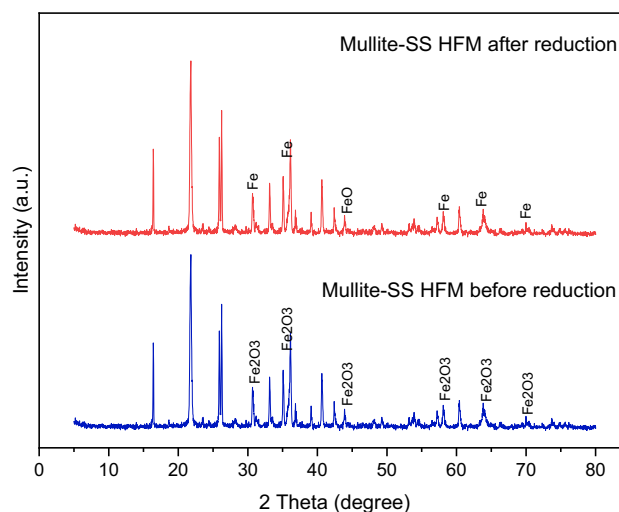**Fig. 8.** Effect of SS contents on rheological characteristics of mullite-SS dopes suspension.

Fig. 9. Photographic image of (A) mullite and SS powders, (B) fabricated mullite-SS HFMs with different SS contents (0.0, 2.5, 5.0, 7.5, 10 and 12 % (w/w) SS) by phase inversion/sintering techniques, sintered at 1350 °C.
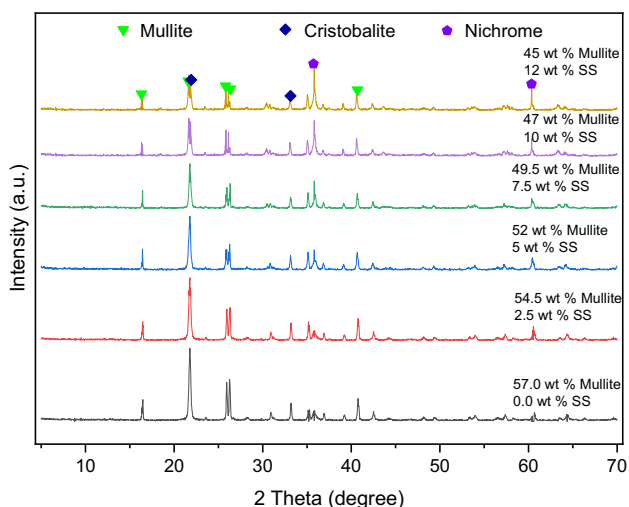
Fig. 10. XRD patterns of mullite-SS HFMs using different SS contents.

Fig. 11. XRD pattern of Fe_2O_3 in the composition of mullite-SS HFM sintered at 1350 °C before and after reduction reaction by H_2.

ther reduced to Fe by increasing the reaction temperature and time. Therefore, the FeO was further decreased to Fe by increasing the reaction temperature to over 800 °C and the reaction time to more than 4 h in the H_2 environment. Based on the obtained outcomes, the proposed technique successfully reduced Fe_2O_3 to Fe.

3.3.2. Physical properties of mullite-SS HFMs

Li [23] reported that to fabricate a ceramic membrane with a well morphological structure, small pore sizes, and well pore sizes distribution, ceramic contents in the dope suspension ranged between 50 and 60 % (w/w). Therefore, several mullite dope suspensions were studied to obtain the best dope suspension that fit the SS contents to form a proper mullite-SS dope suspension with a weight loading between 50 and 60% (w/w). Although Twibi, et al. [5] reported that the best mullite contents in the dope suspension to form mullite hollow fibre membrane was 60% (w/w). However, this mullite content of 60 wt% with SS contents had a low fluidity due to extremely high viscosity, affecting the spinnability of the suspension. Thus, we proposed three mullite contents of 57, 54, and 51% (w/w). The phase inversion/sintering technique was applied with the fabrication parameters of a 6 mL/min extrusion rate, a 10 mL/min bore fluid flow rate, an air gap distance of 5 cm and a sintering temperature of 1350 °C. The preparation of mullite-SS HF precursor at these conditions using 54 and 57% (w/w) mullite contents with SS contents showed a suitable dope suspension viscosity of 27.81 and 29.02 pa.s, respectively and well membrane morphology, as depicted in Fig. 12. This dope

suspension viscosity was significantly close to the optimum viscosity of ceramic slurry (28.5 pa.s) that Yanu, et al. [44] reported. On the other hand, at 51 wt% mullite contents with SS contents, the formation of mullite-SS HF precursor was difficult due to the low dope suspension viscosity of 18.34 pa.s. As a result, the dope suspension with the mullite contents of 57 % (w/w) was optimum in this study (Fig. 12).

The optimum mullite-kaolinite loading of 57 % (w/w) was used with different SS contents to prepare mullite-kaolinite/SS HFMs. These membranes were prepared at an extrusion rate of 10 mL/min, a bore fluid flow rate of 10 mL/min, an air gap distance of 5 cm and a sintering temperature of 1350 °C. The SEM images of the cross-section of the mullite-SS HFMs at various contents of SS (i.e., 0.0, 2.5, 5.0,7.5, 10, and 12 % (w/w)) are exhibited in Fig. 13.

All prepared mullite-SS HFMs showed an asymmetric structure due to the phase inversion technique. The formation of the asymmetric structure of the mullite-SS HFMs obeyed the viscous fingering phenomenon reported by Kingsbury and Li [45]. Viscous fingering generally is a hydrodynamic instability that occurs when a less viscous fluid displaces a more viscous fluid in a porous medium to form an asymmetric structure [45]. The asymmetric structure of the mullite-SS HFMs occurred when the pristine mullite-SS HFs containing polymer solution with suspended mullite and SS powders were immersed in the external nonsolvent bath (water bath). During the immersion, the NMP solvent started diffusing out of the pristine mullite-SS HFs, while the nonsolvent started diffusing into the pristine mullite-SS HFs. This exchange of solvent and
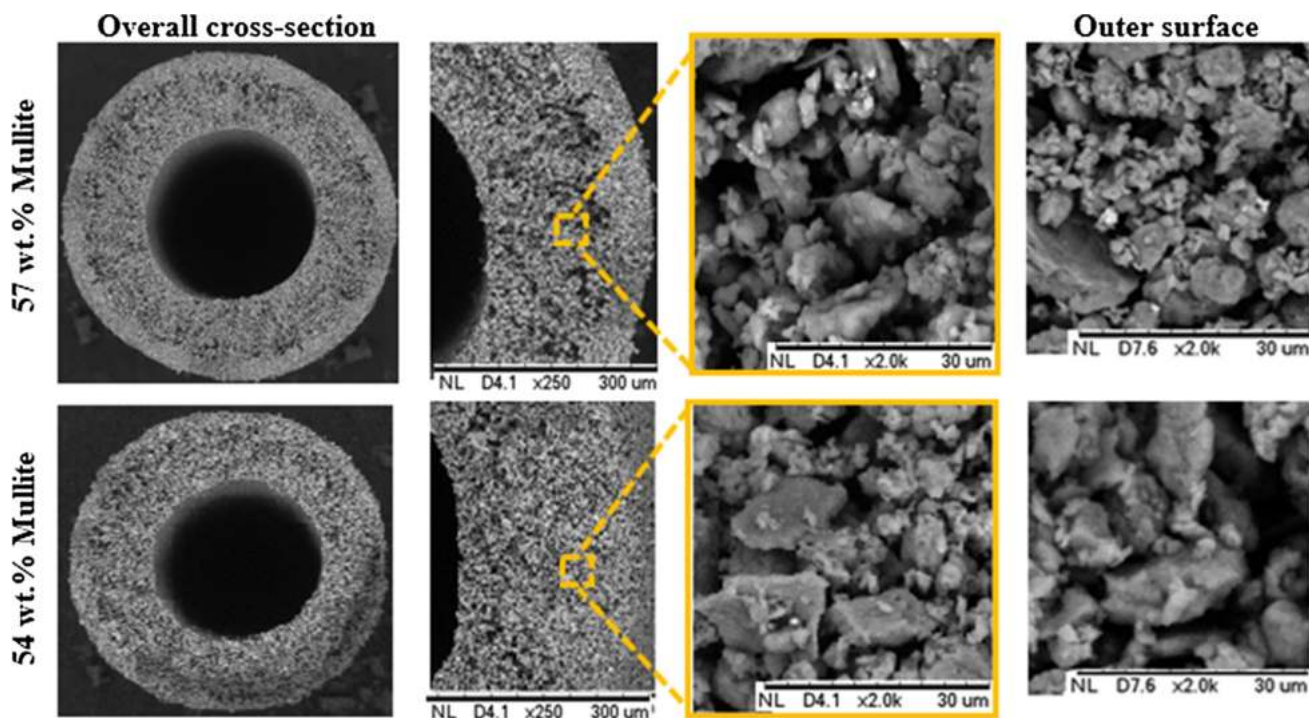
Fig. 12. SEM images of mullite HFMs with different mullite contents of 54 and 57 % (w/w) mullite by phase inversion/sintering techniques, sintered at 1350 °C.

nonsolvent caused the polymer binder in the pristine mullite-SS HFs to shift from a state of thermodynamic stability to a state of metastability or instability, leading to liquid–liquid mixing in the pristine mullite-SS HFs. When the solvent flux was greater than the nonsolvent flux, the polymer concentration at the interface increased, creating a highly concentrated polymer layer at the surface. This layer slowed the exchange rate of solvent and nonsolvent, resulting in a lower polymer concentration in the sublayer than in the top layer. Further substituting solvent with nonsolvent solidifying the polymer-rich phase produced an asymmetric membrane structure [46]. After sintering, the asymmetric structure was preserved, although there were modifications in the voids caused by shrinkage.

In addition, all the developed HFMs exhibit porous structures comprising micro-voids and sponge-like structures HFM, except mullite-SS HFM with 12 % (w/w) SS exhibited only sponge-like structures with very narrow pores. The formation of micro-voids and sponge-like in the cross-section of mullite HFMs agreed with the outcomes reported by the Twibi group [5] and Paiman et al. [40].

Another significant observation from Fig. 13 was that the mullite-SS HFMs containing SS of 0.0, 2.5,5.0 and 7.5 % (w/w) had some macro-voids, their sizes ranging from 47.9 μm to 64.8 μm, as shown in Fig. 14. These macro-voids are usually described as defects to the fabricated membranes because they reduce the mechanical strength of the membrane and rejection performance, as Greenberg, et al. [47] reported. However, the presence of macro-voids reduced the mass transport resistance, allowing better flux performance. In addition, there were no finger-like voids in the inner cross-section of the membrane. This observation could be due to the high viscosity of the dope solutions that inhibited the mechanism of viscous fingering from forming the fingers-like inner membrane structure. This observation was similar to previous studies by Kingsbury and Li [45].

The inner section of the mullite HFM (0.0 % (w/w) SS) had an asymmetrical structure in the membrane cross-section with dominant micro-voids of about 80% of the membrane wall and some

sponge-like about 20 % of the membrane wall and membrane wall thickness of 0.52 mm. However, mullite-SS HFMs had lower micro-voids and higher sponge-like than mullite HFM. The gradual increase of SS contents (2.5, 5.0, 7.5, 10, and 12 % (w/w)) in the mullite-SS HFMs gradually increased the sponge-like and reduced the micro-voids. Adding the SS with different contents reduced the mean pore size of porous mullite and formed a very well network between mullite and SS particles. Regarding the structure, the mullite-SS HFMs with 25% illustrated a similar structure trend of mullite HFM with a slight increase in the sponge-like of 25% and a slight decrease of micro-voids of about 75% and wall thickness of about 0.50 mm. The mullite-SS HFMs with 5 and 7.5 % (w/w) SS demonstrated almost a similar trend of asymmetric structure where the formation of micro-voids decreased to about 60%, while the remaining pores of about 40% of the wall thickness were sponge-like. On the other hand, these two membranes showed different cross-section thicknesses of 0.49 and 0.48 mm, respectively. The mullite-SS HFMs with 10% (w/w) SS showed a sponge-like of about 80%, micro-voids of about 20%, and a membrane cross-section of 0.43 mm. In contrast, no micro-voids were observed for the mullite-SS HFMs with 12% (w/w) SS. Only the sponge-like structure with narrow pores was obtained with a membrane cross-section of about 0.44 mm.

In addition, Fig. 13 demonstrates that the SS particles were successfully spread between mullite particles, demonstrating a homogenous combination between the mullite and SS particles, as proved by the element distribution mapping presented in Fig. 15. The EDX elemental mapping analysis was used to evaluate the distribution of SS elements within the mullite particles for all mullite-SS HFMs prepared with different SS contents, as displayed in Fig. 15 (A-E). The Figure revealed that silicon (light green) and alumina (dark green) were the most abundant compounds in all prepared mullite-SS HFMs. Moreover, the SS elements, including Fe (purple), Cr (navy blue), Ni (dark blue), and Mo (light blue), were distinctly distributed between the mullite particles in all the fabricated mullite-SS HFMs, demonstrating the successful integration of SS particles with mullite particles and the successful fabrication of
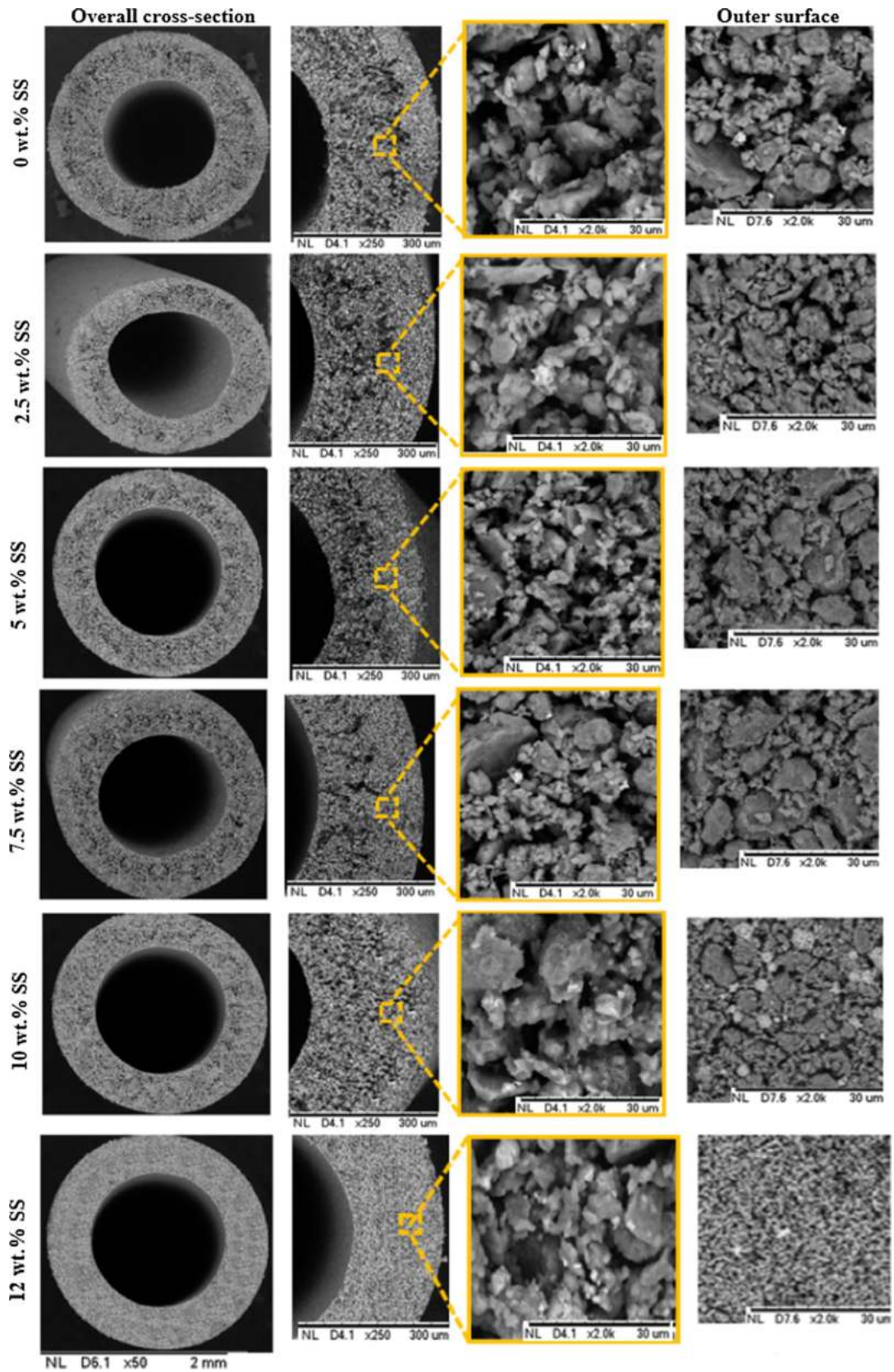
Fig. 13. SEM images of mullite-SS HFMs after the reduction process at different SS contents (i.e., 0.0, 2.5, 5.0, 7.5, 10, and 12 % (w/w)), prepared at an extrusion rate of 10 mL/min, a bore fluid flow rate of 10 mL/min, and an air gap distance of 5, sintered at 1350 °C.
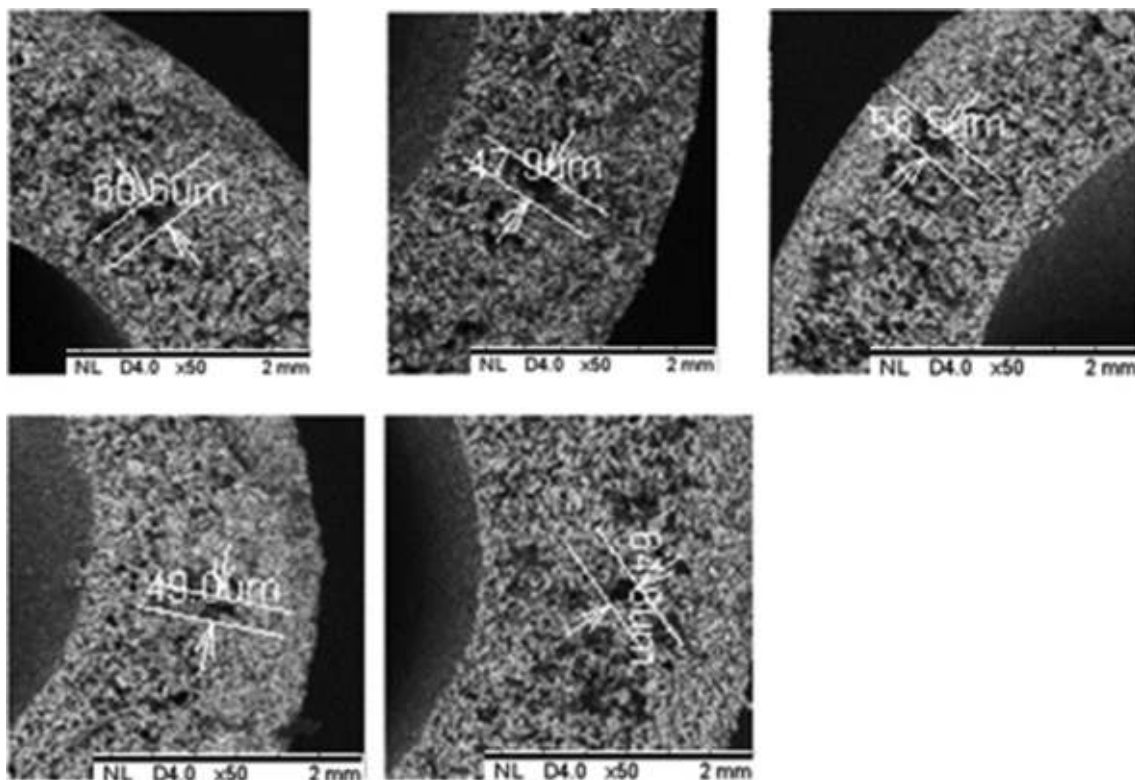
Fig. 14. SEM images of several macro-voids at mullite-SS HFMs containing 0.0, 2.5,5.0 and 7.5 % (w/w) SS, sintered at 1350 °C.

mullite-SS HFMs. A similar trend has been stated by Deng, et al. [39].

The effects of SS contents on the wall thickness, sponge-like, and micro-void layers thickness of mullite-SS HFMs were evaluated by SEM analysis and are summarised in Table 4.

Fig. 13 also displays the effects of SS contents on the outer surface morphology of the mullite-SS HFMs at 1350 °C sintering temperature. The non-uniform interconnecting grain size formation was observed with open pores for all HFMs. The most open pores were observed at HFMs with 0 % (w/w) SS. With increased SS contents from 0 to 12 % (w/w), these open pores generally decreased gradually because of increased SS particles between mullite particles and higher necks growth formation between these particles at the sintering process. At the HFMs with 5.0 and 7.5, 10 % (w/w) SS, there was a slight change in the outer membrane surface pores, while at HFMs with 12 % (w/w), the narrowest pores were observed.

Many sintering process conditions, such as high sintering temperatures and long-time sintering processes, can effectively increase the bending strength of mullite HFMs. On the other hand, these sintering conditions caused high porosity and pore size reduction, resulting in membrane densification [6]. Moreover, the sintering process in the presence of the nanoparticle particles used as a support material to enhance the bending strength of HFMs is difficult to control during the sintering process [48]. Therefore, this study used SS powder with particle sizes of 3 μm to increase the bending strength of mullite HFMs fabricated by mullite powder with a particle size of 18 μm. The main function of the SS particles was to fill in the large voids between mullite particles to improve the bending strength of the mullite HFM, as shown in Fig. 16.

Membrane mechanical stability was significant in membrane filtration processes. Fig. 17 exhibits the bending strength assessment outcomes of the mullite-SS HFMs fabricated with different SS contents and sintered at 1350 °C for 6 h. The bending strength

of mullite-SS HFMs was improved with increased SS contents over the mullite HFMs. The increase in the SS contents from 0.0, 2.5, 5.0, 7.5, 10, and 12% (w/w) improved the bending strength of mullite-SS HFMs to 32.1, 38.4, 45.2, 58.6, 66.7 and 79.8 MPa, respectively. This observation is similar to the outcomes of Deng, et al. [39], who reported that the gradual increase in the titania (TiO$_2$) content in the mullite HFMs from 0 to 9 wt% led to a gradual improvement in the bending strength from 11 to 12.5 MPa, respectively.

Another significant observation was that the lowest mechanical strength of 32.1 MPa was observed for the mullite HFM with 0 % (w/w) SS. The very low mechanical strength could be attributed to weak packed particles of mullite particles that composed the mullite HFM due to the low sintering temperature, as Zhu, et al. [49] reported in their study for the fabrication of mullite-titania HFM.

Moreover, this low bending strength of mullite HFM at a low sintering temperature was evidenced by Twibi, et al. [5] for mullite-kaolinite HFMs. However, at the sintering temperature of 1350 °C, the highest mechanical strength of 66.7 and 79.8 MPa was found at mullite-SS HFM with 10 and 12 % (w/w) SS, respectively, due to the well-symmetric structure with sponge-like voids due to the good integration between mullite and SS particles. According to Li, et al. [11], the sponge-like region in the membrane cross-section represented a mechanical strength higher than that of the figure-like regain. In addition, SS particles acted as a reinforcement phase improving the bending strength and the packing structure of porous mullite-SS HFMs. This observation agreed with the observed trend in the SEM micrographs shown in Fig. 13. The high mechanical strength of mullite-SS HFMs significantly reduced the chance of membrane failure in separation and filtration processes for long-term operation.
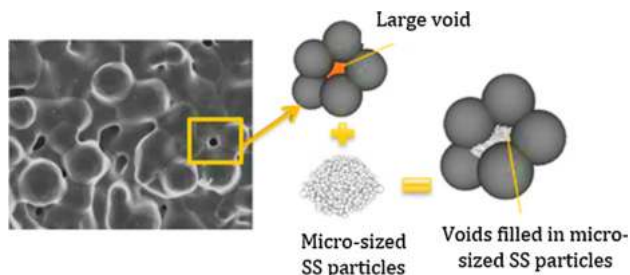
The effects of SS contents on the mean pore size, porosity, and pore size distribution of mullite-SS HFMs sintered at 1350 °C are shown in Fig. 18 A and B. Fig. 18 A demonstrates that the porosity
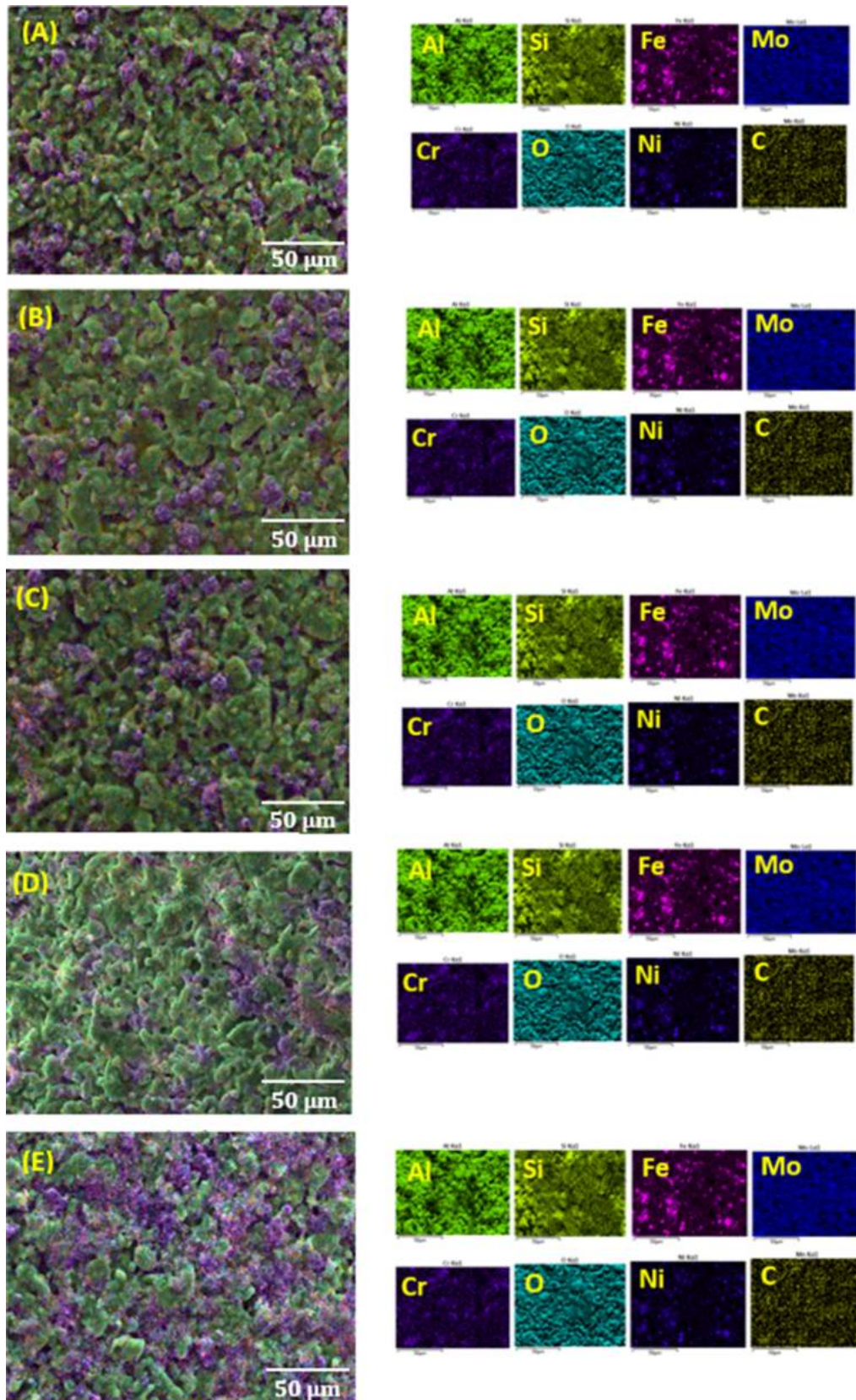
Fig. 15. EDX elemental mapping analysis on the cross-section of mullite-SS HFMs of (A) M-SS,2.5 wt% SS, (B) M-SS, 5 wt% SS, (C) M-SS,7.5 wt% SS, (D) M-SS, 10 wt% SS and (E) M-SS, 12 wt% SS.

Table 4
Effects of SS contents on the membranes wall thickness, sponge-like and micro-void layers thickness.

SS contents wt.%	Sponge-like layer thickness (%)	Micro-voids layer thickness (%)	Wall thickness (mm)
0	20	80	0.451
2.5	25	75	0.435
5	40	60	0.411
7.5	60	40	0.389
10	90	10	0.365
12	100	0	0.326

Fig. 16. Sketch diagram of filling the large mullite voids by micro-sized SS particles, modified from Chong et al. [48].
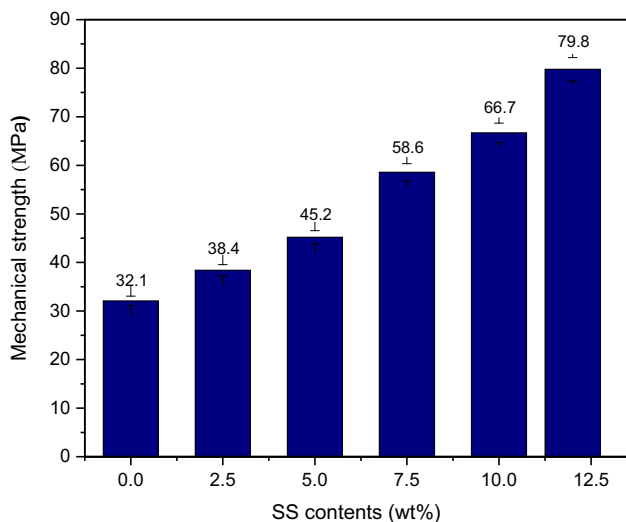
Fig. 17. Mechanical strengths of mullite-SS HFMs at different SS contents, sintered at 1350 °C [notice: error bars are based on standard errors from three duplicate calculations].

of all mullite-SS HFMs reduced gradually with increasing the SS contents, while the mean pore size at the SS contents of 0, 2.5, 5.0, and 12 % (w/w) had a sharp decrease to 0.75, 0.69 and 0.63 μm respectively, but at SS contents of 7.5 and 10 % (w/w) SS had a slight decrease in the mean pore size to 0.61, and 0.59 μm, respectively. The largest mean pore size of 0.75 μm and highest porosity of 36.1 % was observed at the mullite-SS HFM with 0 % (w/w) SS (mullite HFM). This note could be due to the large pores of the mullite HFM. In contrast, the mullite-SS HFM with 12 % (w/w) SS showed the smallest mean pore size of 0.30 μm and the lowest porosity of 19.9 %. The porosity of rest membranes with SS contents of 2.5, 5.0, and 7.5 % SS was 35.5, 32.6, and 31.6 %, respectively. This finding agreed with a previous work by Deng, et al. [39]. Another significant observation was that the range of porosity of all mullite-SS HFMs was from 19.9 to 36.1 %, as Fung

and Wang [50] recommended that the optimum porosity of ceramic membrane ranged from 30 to 90 %.

Fig. 18 B exhibits the effects of the different SS contents on the pore size distribution of the mullite-SS HFMs. All pore size distribution curves of mullite-SS HFMS exhibited almost the same width and binominal pore size distribution. All membranes' overall pore size varied from 0.01 μm to 1.95 μm. In addition, all pore size distribution curves demonstrated small pore size, mostly related to the sponge-like structure, as evidenced in Fig. 7. For mullite-SS HFM at 0.0 % (w/w) SS, the highest pore peak was observed at a pore size of 0.59 μm, while at the membrane with 12 % (w/w) SS, the lowest pore peak was observed at a pore diameter of 0.32 μm. Increasing the SS contents to 2.5, 5.0, 7.5, and 10 % (w/w) SS resulted in a change of the pore peaks to 0.42, 0.31, 0.43 and 0.42 μm, respectively. Decreasing the heights of the pore peaks indicates that the number of pores becomes less. This notice could be due to the increasing SS contents in the mullite-SS HFMs. Furthermore, it can be observed that the highest pore peaks for mullite-SS HFMs with 2.5, 7.5, and 10 % (w/w) SS were at the same pore diameter at 0.43 μm. This observation was observed in many previous works in literature [6,11,50].

Hydrophilic membranes with a high hydrophilic property are significantly desired in many filtration applications, such as oil/water separation. These membranes mainly allowed water to pass the membrane pores while efficiently rejecting oil from passing depending on the degree of membrane hydrophilicity, which typically depended on the membrane pores size, as Mohtor, et al. [51] explained in their experiment work. Fig. 19 shows the average water and oil contact angle values on the surface of mullite-SS HFMs fabricated by different SS contents (i.e., 0.0, 2.5, 5.0, 7.5, 10, and 12 % (w/w)). As seen in Fig. 19 (A&B), the water contact angles of mullite HFM and mullite-SS HFMs were zero due to the quick spread of water into the members, causing a difficult measurement of the water contact angle values.

In addition, water drops could not remain on the membrane surface due to the high hydrophilicity of the membranes due to the large pores size of mullite-SS HFMs that allows fast water penetration. Another significant observation was that increased SS contents did not affect all mullite-SS HFMs water contact angles and remained zero. This observation was similar to that mentioned elsewhere [5,6]. However, the oil drops on the mullite-SS HFMs had a lower spread on the membrane surface than water, resulting in readable contact angles, as shown in Fig. 19 (C-G). The gradual increase of the SS contents from 0.0, 2.5, 5.0, 7.5 to 10 % (w/w) caused a gradual increase in the oil contact angle from 31.2°, 35.4°, 41.1°, and 44.0° to 49.8°. This increase in the oil contact angle was attributed to the function of SS powders that reduced the large pores size of mullite HFMs and increased the membrane roughness.

This study proposed that the SS content of 10% (w/w) was the optimum SS content for mullite-SS HFM fabrication because of its well-structured membrane morphology with sponge-like structure, free of macro-void defects, higher bending strength, small pore sizes and good porosity. Thus, it was selected to be the optimum for investigating the impact of the bore fluid flow rate and air–gap distance on the morphology and bending strength of mullite-SS HFMs.

According to Kingsbury and Li [45], the variation in spinning parameters such as bore fluid rate and air–gap distance significantly affected the membrane morphology and bending strength. Fig. 20 demonstrates the SEM images of effecting various bore fluid flow rates of 4, 6, 8, and 10 mL/min on the mullite-SS HFM morphology at a fixed air–gap of 5 cm and an extrusion rate of 10 mL/min. In the phase inversion process of the mullite-SS dope solution, shrinkage was noted due to the diffusion rate of distilled water into the dope suspension being slower than the diffusion
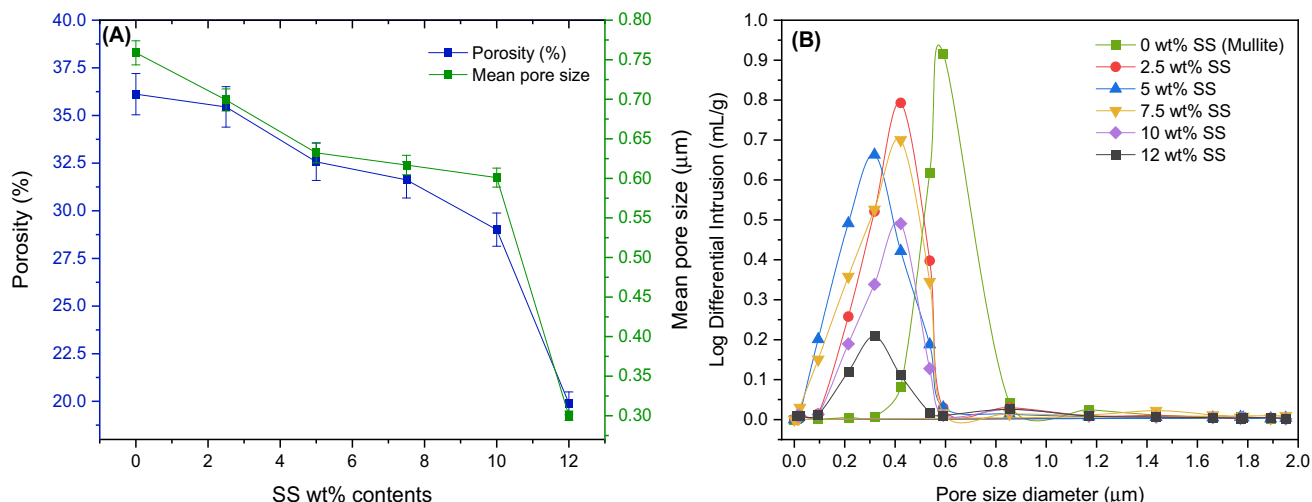
Fig. 18. (A) mean pore size and porosity, (B) pore size distribution of mullite-SS HFMs at different SS contents, sintered at 1350 °C by MIP analysis [notice: error bars are based on standard errors from three duplicate calculations].


Fig. 19. Water and oil contact angles of mullite-SS HFMs at different SS contents, sintered at 1350 °C.

rate of the NMP solvent. As a result of shrinkage, the internal radial force was generated and caused a deformation of the inner membrane structure. This trend was observed in the literature [11,52].

By comparison, the deformation of the inner structure of mullite-SS HFM presented in Fig. 20 showed a clear difference in the degree of deformation depending on the bore fluid flow rates. For example, the increase in the bore fluid flow rates of the resultant mullite-SS from the spinning process from 4, 6, 8, and 10 mL/min caused a gradual decrease in the solidification rate in the inner membrane structure. In addition, it increased the inner membrane

diameter from 0.03, 1.10, and 1.98 to 2.21 mm, respectively, as shown in Fig. 20 (A), (B), (C), and (D). As a result of increasing the membrane diameter, the membrane bending strength decreased gradually from 89.62, 77.13, 68.02, and 66.74 MPa (Fig. 21). This observation had a similar trend in the literature for increasing mechanical strength and decreasing membrane diameter [53,54].

At 4, 6, and 8 mL/min, the bore fluid flow rate was insufficient to provide a strong hydrodynamic force against the mullite-SS dope solution during the spinning process to interchange solvents
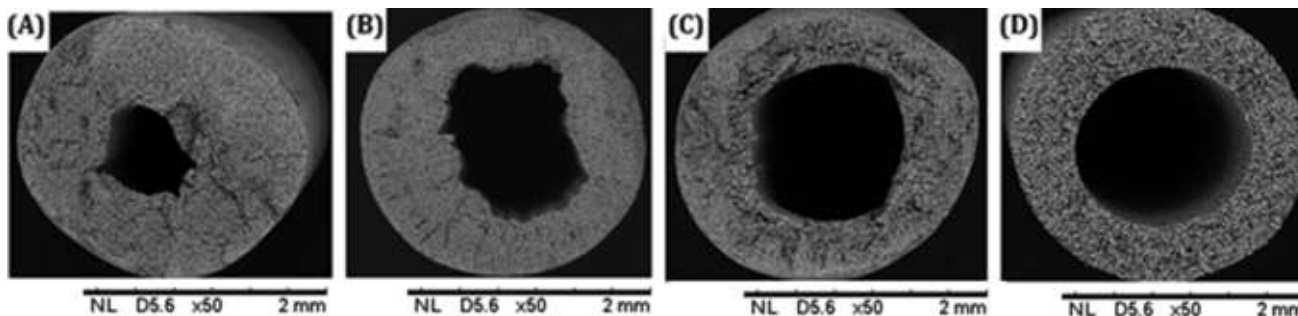
Fig. 20. SEM images of the mullite-SS HFMs with 10 % (w/w) SS at various bore fluid flow rates: (A) 4 mL/min, (B) 6 mL/min, (C) 8 mL/min, (D) 10 mL/min, at an air–gap of 5 cm, sintered at 1350 °C.
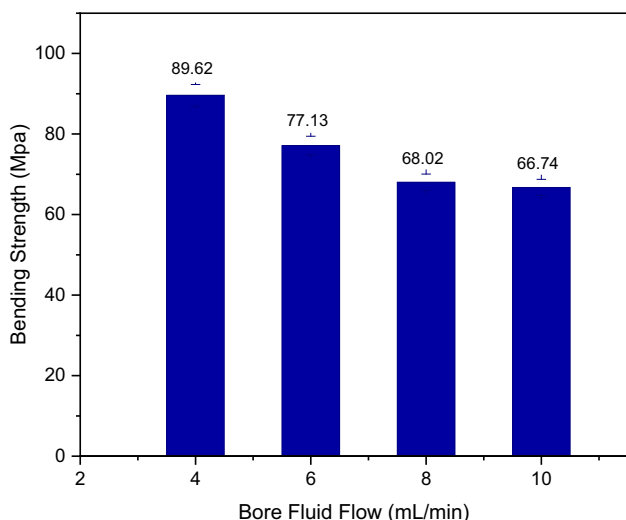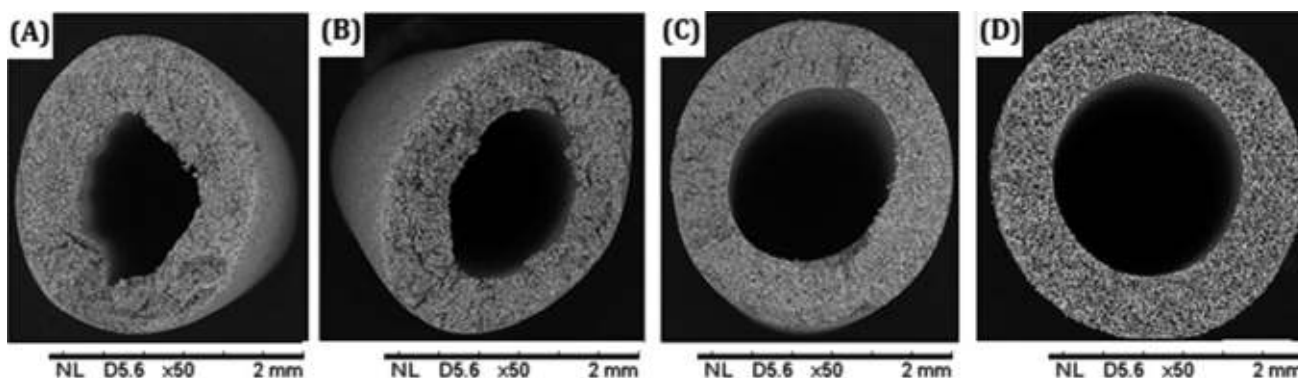

Fig. 21. Mechanical strength of mullite-SS with 10 % (w/w) SS fabricated at different bore fluid flow rates, sintered at 1350 °C [notice: error bars are based on standard errors from three duplicate calculations].

(NMP) and nonsolvents (distilled water), resulting in partial polymer solidification on the inner lumen of the resultant mullite-SS HF. However, at a 10 mL/min bore fluid flow rate, a complete polymer solidification was formed on the inner membrane surface due to sufficient hydrodynamic force applied against the mullite-SS dope solution. Consequently, a good morphology was formed, as represented in Fig. 21 (D), and lower bending strength was obtained at 66.74 MPa, as shown in Fig. 21. This trend agreed with the finding obtained by Li et al. experimental work [11].

In addition, the membrane morphology and mechanical strength were evaluated at different air–gap distances of 5, 10, 15, and 20 cm at a fixed bore fluid flow rate of 10 mL/min and an extrusion rate of 10 mL/min. As seen in Fig. 22 (A, B, C, and D), the principal effect of the air–gap distance was on the morphological structure of the membrane, which affected the membrane wall thickness and resulted in an effect on the membrane bending strength. Furthermore, increasing the air–gap distance caused more deformation on the membrane cross-section with large micro-voids because of the long contact time between distilled water (inside coagulant) and air with the resultant mullite-SS HF, which increased the viscosity of the outer surface due to the solvent evaporation and moisture condensed on the membrane surface at the same time. The largest deformation in the membrane cross-section was observed at the air–gap distance of 20 cm, while the best morphological structure was seen at the lowest air–gap distance of 5 cm. These findings were also reported in the literature [5,55].

However, the membrane bending strength depended on the membrane cross-section thickness that resulted from different air–gap distances, as shown in Fig. 23. The highest bending strength of 66.74 was recorded at the lowest air–gap distance of 5 cm. In contrast, the other bending strength of 64.30, 64.02, and 61.41 MPa was observed at air–gap distances of 10, 15, and 20 cm, respectively. Another interesting observation was a slight difference in the bending strength at the air–gap distances of 10 and 15 cm, while at 20 cm, the lowest bending strength of 61.41 MPa was noted. These findings are similar to Gitis and Rothenberg's findings. They revealed that increasing the membrane cross-section thickness increases the bending strength of the membrane and its mechanical stability.

Overall, this concluded that the optimum air gap distance and bore fluid flow rate that provided the optimum membrane mor-

Fig. 22. SEM images of mullite-SS HFMs with 10 % (w/w) SS fabricated at different air–gap distances (A) 20 cm, (B) 15 cm, (C) 10 cm, (D) 5 cm, at a bore fluid flow rate of 10 mL/min, and sintered at 1350 °C.
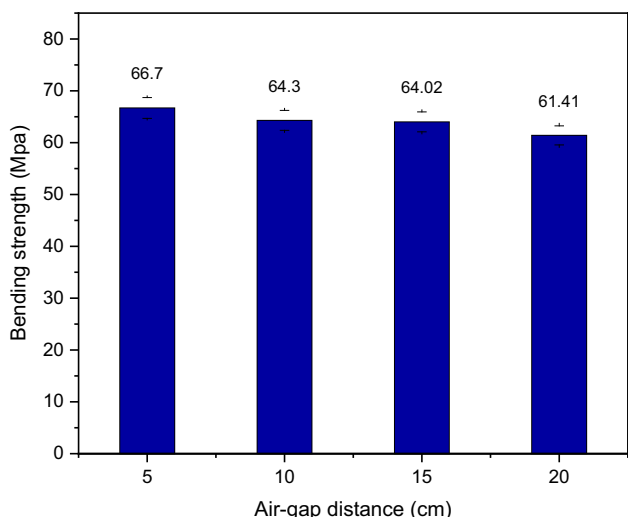
Fig. 23. Mechanical strengths of mullite-SS HFMs with 10 % (w/w) SS fabricated at different air–gap distances and sintered at 1350 °C [notice: error bars are based on standard errors from three duplicate calculations].

phology and structure for mullite-SS HFMs were at 5 cm and 10 mL/min, respectively. As a result, the mullite-SS HFMs were prepared at these fabrication parameters and employed for the pure water permeation oil/water separation process in this study.

3.4. Effect of SS contents on pure water permeation

The effect of SS contents on the permeation of pure water through mullite-SS HFMs was investigated and evaluated by a crossflow filtration system at 2 bar pressure using pure distillate water for 90 min, and the results are exhibited in Fig. 24. The highest water permeation of 460 L/m² h was observed for mullite HFM with 0 wt% SS, while the lowest water permeation of 185 L/m² h was recorded at the mullite-SS HFM with 12 wt% SS. Besides, increasing time showed almost steady-state water permeation for all mullite-SS HFMs at first 40 min, while the mullite-SS HFM with 12 wt% SS showed at first 20 min. This observation could be attributed to the high hydrophilicity of all mullite-SS HFMs based on the contact angle measurement. Because of the high hydroxyl
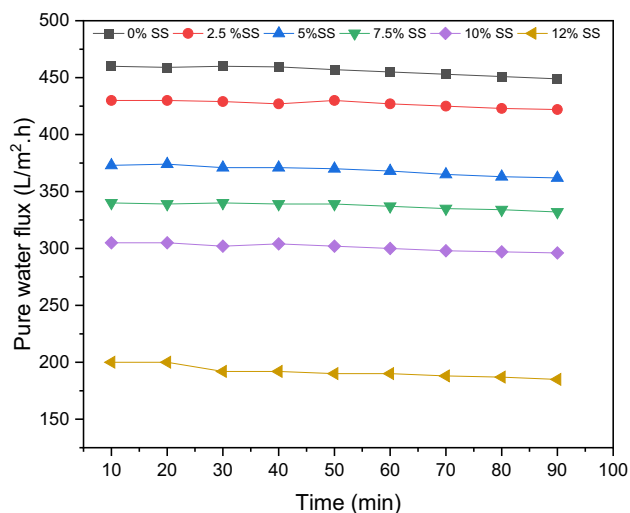
groups from the ceramic material (mullite) on all mullite-SS HFMs, the membranes absorb water droplets instantly after reaching the membrane surface, facilitating quick water flow through the membranes [1].

Another significant observation was that after 50 min, there was a slight reduction in water permeation for all mullite-SS HFMs except mullite-SS HFM with 12 wt% SS showed after 20 min. This could be due to the interaction of mullite molecules with water molecules on the membrane surface, which resulted in a slight saturation of the membrane pores and a slight increase of the membrane resistance for water molecules, as reported in previous experimental work [5]. In addition, as can be seen from the Figure, there was an obvious gap in pure water flux between mullite-SS HFMs fabricated with 12 wt% SS and other membranes fabricated with other SS contents. This observation could be attributed to the tight pores and low porosity due to the high SS contents between mullite particles.

3.5. Performance test of mullite-SS HFMs for oil/water separation

Fung and Wang [56] reported that adding reinforcement materials to ceramic membranes generally reduces the water flux, increases the rejection rates, and increases the mechanical properties of membranes. This claim was observed in this study by increasing the SS contents from 0.0, 2.5, 5.0, 7.5, and 10 to 12% (w/w), and the relationship between the water flux and the SS contents is shown in Fig. 25. The flux of water through mullite-SS HFMs was investigated and evaluated at the sintering temperature of 1350 °C and 2 bar pressure. As reflected by the Figure, the increment of the SS content significantly impacted the water flux with time for all mullite-SS HFMs.

Overall, the mullite HFMs with 0 % (w/w) SS showed the highest water flux of 460 L/m2.h at the first 10 min. Meanwhile, a gradual reduction in the water flux with time was observed with increasing SS contents from 0 to 12 % (w/w), where the lowest water flux of 290 L/m2.h was obtained for mullite-SS HFMs with 12% (w/w) SS at the period. A higher SS content could decrease the water flux due to a significant change in the membrane pores size and porosity due to increased SS contents, as shown in Fig. 17.

In addition, all HFMs showed a sharp reduction in the water flux with a time between 10 and 50 min. This could be attributed to the mullite-SS molecular interaction with water molecules on the membrane surface, which resulted in the saturation of membrane
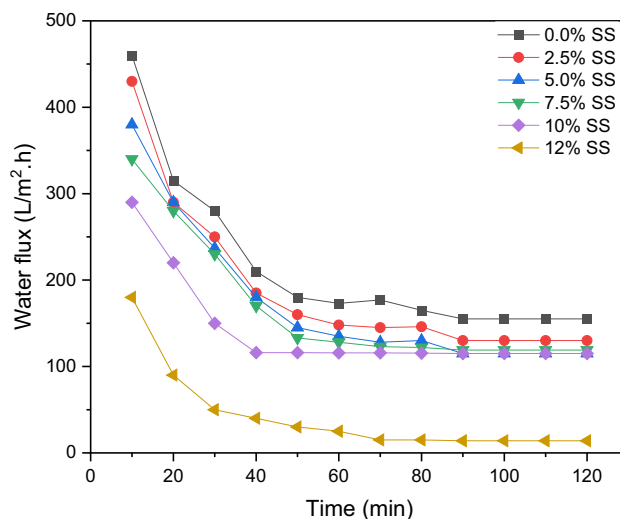

Fig. 24. Water permeation of mullite-SS HFMs at different SS content, sintered at 1350 °C.

Fig. 25. Water flux of mullite-SS HFMs at different SS content sintered at 1350 °C [notice: error bars are based on standard errors from three duplicate calculations].

pores and increased the membrane resistance for water molecules, as reported in previous experimental work [5]. The highest stable water flux of 155 L/m² h was also observed for mullite HFM behind 90 min, while the lowest stable water flux of 115 L/m² h was recorded at the mullite-SS HFM with 10 wt% SS. No steady-state water flux was observed for the membranes with the SS contents of 0.0, 2.5 and 5.0 % (w/w) before 90 min, whereas for mullite-SS HFMs with 7.5, 10 and 12 % (w/w), SS was observed. For mullite-SS HFM with 7.5 % (w/w) SS, steady-state water flux was observed after 50 min and continued until the end of the filtration process at 120 min with a water flux of 119 L/m² h. In comparison, for mullite-SS HFMs with 10 and 12 % (w/w) SS, steady-state water flux was observed at a minute after 60 and 70 min, respectively and remained constant until the end of the filtration process at 120 min with a water flux of 115 and 13 L/m² h.

Another significant observation was an obvious gap in the water flux between mullite-SS HFMs fabricated with 0.0, 2.5, 5.0 and 7.5 % (w/w) SS and the mullite-SS HFMs fabricated with 10 % (w/w) SS at the first 40 min. This observation could be attributed to the sponge-like and micro-void structures formed in the cross-section of the membrane containing 0.0, 2.5, 5.0 and 7.5 % (w/w) SS (Fig. 11) and the formation of some macro-void structures, as shown by the SEM images in Fig. 20. As a result, it is proposed that the micro-void and macro-void structures could increase the water permeation and cause unsteady-state water permeation. Besides, there was an obvious gap in the water flux between mullite-SS HFMs with 10 % (w/w) SS and the mullite-SS HFMs with 12 % (w/w) SS from the first 10 min until 120 min. This gap could be

attributed to the higher contents of SS that resulted in a reduction in pore sizes and membrane porosity. This result was similar to that of a study undertaken by Deng, et al. [39].

The rejection performance of the mullite-SS HFMs fabricated at different SS contents to separate oil/water with different oil concentrations (i.e. 1000, 1500, and 2000 ppm) is shown in Fig. 26. The oil rejection performance increased by about 10.5 %, increasing the SS contents from 0 to 10% (w/w). The gradual increase in the SS contents increased the oil rejection for all oily wastewater emulations. The highest oil rejection of 96.9 and 100 % was achieved by mullite-SS HFM with 10 and 12 % (w/w) SS, respectively, at 1000 ppm, while the lowest oil rejection of 88 % was reported for mullite-SS HFM with 0 % (w/w) SS at the same concentration. This phenomenon was noted with all other emulsions of 1500 and 2000 ppm (Fig. 24). The decline of the oil particles was much improved at 12 % (w/w) SS over other mullite-SS HFM prepared at other SS contents (i.e., 0–10 % (w/w)) due to its much smaller pores size, lower porosity and much denser pores structure, which retained the oil particles at the feed side [57–59]. Besides, it could be due to the blockage of some membrane pores due to the high SS contents. Furthermore, the increase in the oil concentration from 1000, 1500, to 2000 ppm increased the viscosity of the feed solution and reduced the oil rejection performance. This observation could be attributed to the highly emulsified oil particles in the oil/water emulations, which enabled oil to drop on the membrane surface as a cake layer and increased the resistance of the membrane surface against water permeation. This behaviour was observed elsewhere in the literature [60]. As a result, the synthesized mullite-SS HFM with 10% (w/w) could serve as a proper choice for oil/water separation.
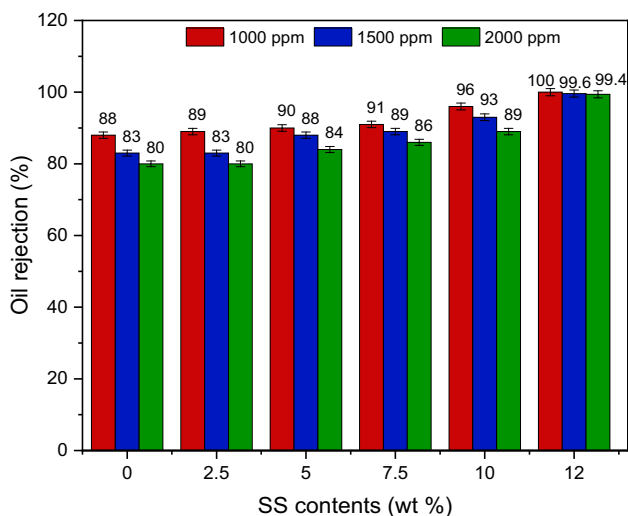
4. Comparison of the mullite-SS HFM performance with other mullite and kaolin HFMs

The mullite-SS HFM performance for oil rejection from oil/water emulsion was evaluated and compared with other mullite and kaolin HFMs. As presented in Table 5, the mullite-SS HFMs showed a high permeation flux and an excellent oil rejection rate. The oil rejection rate of mullite-SS HFMs with 10 % (w/w) SS sintered at 1350 °C was the same as that of mullite-kaolinite sintered at 1450 °C. Since all mullite and kaolin HFMs usually could not stand for long-time filtration processes due to their low mechanical strength. As a result, the mullite-SS HFMs were an excellent alternative for oil/water separation due to their good bending strength of 66.74 MPa, as compared to other mullite and kaolin HFMs sintered at the same sintering temperature.

5. Conclusion

This study has demonstrated that mullite-SS HFMs with sponge-like and asymmetric structures were successfully synthesized in this study by mullite and SS loading of 57% (w/w), an

Fig. 26. Oil rejection performance by mullite-SS HFMs fabricated from different SS contents [notice: error bars are based on standard errors from three duplicate calculations].

Table 5
Comparison between mullite-SS HFM with mullite and kaolin HFMs.

Membrane material	SS content (wt.%)	Ceramic content (wt.%)	Sintering temperature (°C)	Mechanical strength (MPa)	Porosity (%)	Water permeation (L/ m² h)	Oil rejection rate (%)	Ref.
Kaolin	–	37.5	1500	93.2	5.2	35.0	100	[41]
Al₂O₃-kaolin	–	50.0	1600	10.8	–	–	–	[61]
Kaolin	–	35.0	1300	15	58.0	320	91.8	[62]
Mullite (coal-gangue)	–	–	1400	34	47.2	35.8	97.0	[63]
Mullite-kaolinite	–	60.0	1450	78	10.8	182	97.1	[5]
Mullite-SS	10	47.0	1350	66.7	29.0	290	96.9	This work

extrusion rate of 6 mL/min, a bore fluid flow of 10 mL/min and different SS contents of 0.0, 2.5, 5.0, 7.5, 10 and 12 % (w/w) SS by inversion/sintering techniques. The SS particles successfully filled the gaps between the mullite particles and formed a good bending strength between membrane particles at a sintering temperature of 1350 °C. The increased SS contents from 0.0, 2.5, 5.0, 7.5, 10 and 12 % (w/w) significantly affected the mechanical properties and increased the bending strengths from 32.1, 38.4, 35.2, 58.6 and 66.7 to 79.8 MPa, respectively. At SS content of 10% (w/w), the mullite-SS HFM showed better physical properties than other membranes after balancing all its physical properties and comparing them with other mullite-SS HFMs containing 0.0, 2.5, 5.0, 7.5 and 12 % (w/w) SS. "Hence, this study has concluded that the 316L SS alloy has the ability to improve the bending strength of mullite HFMs. This study suggests that mullite-SS HFMs can effectively use for oil/water separation.

Declaration of Competing Interest

The authors declare that they have no known competing financial interests or personal relationships that could have appeared to influence the work reported in this paper.

Acknowledgement

References

[1] Zamora-Ledezma C et al. Heavy metal water pollution: A fresh look about hazards, novel and conventional remediation methods. Environ Technol Innov 2021;22:101504.
[2] Omar NMA et al. Recent progress, bottlenecks, improvement strategies and the way forward of membrane distillation technology for arsenic removal from water: a review. J Water Process Eng 2023;52:103504.
[3] Larsen TA, Riechmann ME, Udert KM. State of the art of urine treatment technologies: a critical review. Water Research X 2021;13:100114.
[4] Omar NMA et al. Bottlenecks and recent improvement strategies of ceramic membranes in membrane distillation applications: a review. J Eur Ceram Soc 2022.
[5] Twibi MF et al. Development of high strength, porous mullite ceramic hollow fiber membrane for treatment of oily wastewater. Ceram Int 2021;47 (11):15367–82.
[6] Alftessi SA et al. Novel silica sand hollow fibre ceramic membrane for oily wastewater treatment. J Environ Chem Eng 2021;9(1):104975.
[7] Rasouli S, Rezaei N, Hamedi H, Zendehboudi S, Duan X. Superhydrophobic and superoleophilic membranes for oil-water separation application: a comprehensive review. Mater Des 2021;204:109599.
[8] Lahiere RJ, Goodboy KP. Ceramic membrane treatment of petrochemical wastewater. Environ Prog 1993;12(2):86–96.
[9] Dong Y, Feng X, Feng X, Ding Y, Liu X, Meng G. Preparation of low-cost mullite ceramics from natural bauxite and industrial waste fly ash. J Alloy Compd 2008;460(1–2):599–606.
[10] Suresh K, Pugazhenthi G, Uppaluri R. Fly ash based ceramic microfiltration membranes for oil-water emulsion treatment: Parametric optimization using response surface methodology. J Water Process Eng 2016;13:27–43.
[11] Li L et al. A low-cost alumina-mullite composite hollow fiber ceramic membrane fabricated via phase-inversion and sintering method. J Eur Ceram Soc 2016;36(8):2057–66.
[12] Hubadillah SK, Othman MHD, Harun Z, Ismail A, Rahman MA, Jaafar J. A novel green ceramic hollow fiber membrane (CHFM) derived from rice husk ash as combined adsorbent-separator for efficient heavy metals removal. Ceram Int 2017;43(5):4716–20.
[13] Abd Aziz MH, Othman MHD, Hashim NA, Adam MR, Mustafa A. Fabrication and characterization of mullite ceramic hollow fiber membrane from natural occurring ball clay. Appl Clay Sci 2019;177:51–62.
[14] Roy R, Das D, Rout PK. A review of advanced mullite ceramics. Engineered Science 2021;18:20–30.
[15] Chakraborty AK. Phase transformation of kaolinite clay. Springer; 2014.
[16] D. R. Schmeda-Lopez, S. Smart, W. A. Meulenberg, and J. C. D. da Costa, "Mixed matrix carbon stainless steel (MMCSS) hollow fibres for gas separation," separation and purification technology, vol. 174, pp. 150-158, 2017.
[17] Duke M, Rudolph V, Lu G, Diniz da Costa J. Scale-up of molecular sieve silica membranes for reformate purification. AIChE J 2004;50(10):2630–4.
[18] Fan Z et al. Preparation and properties of a low-cost porous ceramic support from low-grade palygorskite clay and silicon-carbide with vanadium pentoxide additives. Chin J Chem Eng 2021;29:417–25.
[19] Wang YH, Chen G, Wang ZS, Liu JW, Luo PF. Improvement of microcracks resistance of porous aluminium titanate ceramic membrane support using attapulgite clay as additive. Ceram Int 2018;44(2):2077–84.
[20] Fukushima M, Zhou Y, Yoshizawa Y-I. Fabrication and microstructural characterization of porous SiC membrane supports with Al2O3–Y2O3 additives. J Membr Sci 2009;339(1–2):78–84.
[21] Kang H, Sharma A, Jung JP. Recent progress in transient liquid phase and wire bonding technologies for power electronics. Metals 2020;10(7):934.
[22] Khan MI et al. The pyrolysis kinetics of the conversion of Malaysian kaolin to metakaolin. Appl Clay Sci 2017;146:152–61.
[23] Li K. Ceramic membranes for separation and reaction. John Wiley & Sons; 2007.
[24] Hubadillah SK et al. Superhydrophilic, low cost kaolin-based hollow fibre membranes for efficient oily-wastewater separation. Mater Lett 2017;191:119–22.
[25] Tai ZS et al. Design and characterization of ceramic hollow fiber membrane derived from waste ash using phase inversion-based extrusion/sintering technique for water filtration. J Asian Ceram Soc 2021;9(1):341–58.
[26] M. I. B. M. ESHAM, "BAUXITE-BASED HOLLOW FIBER MEMBRANE FOR OILFIELD PRODUCED WATER TREATMENT," Universiti Teknologi Malaysia, 2019.
[27] Rui W, Zhang C, Cai C, Gu X. Effects of sintering atmospheres on properties of stainless steel porous hollow fiber membranes. J Membr Sci 2015;489:90–7.
[28] Raji YO et al. Fabrication of magnesium bentonite hollow fibre ceramic membrane for oil-water separation. Arab J Chem 2020;13(7):5996–6008.
[29] Tai ZS et al. Influence of pre-treatment temperature of palm oil fuel ash on the properties and performance of green ceramic hollow fiber membranes towards oil/water separation application. Sep Purif Technol 2019;222:264–77.
[30] Jamalludin MR, Harun Z, Othman MHD, Hubadillah SK, Yunos MZ, Ismail AF. Morphology and property study of green ceramic hollow fiber membrane derived from waste sugarcane bagasse ash (WSBA). Ceram Int 2018;44 (15):18450–61.
[31] Elaiopoulos K, Perraki T, Grigoropoulou E. Monitoring the effect of hydrothermal treatments on the structure of a natural zeolite through a combined XRD, FTIR, XRF, SEM and N2-porosimetry analysis. Microporous Mesoporous Mater 2010;134(1–3):29–43.
[32] Kamarudin NH et al. Waste environmental sources of metakaolin and corn cob ash for preparation and characterization of green ceramic hollow fibre membrane (h-MCa) for oil-water separation. Ceram Int 2020;46(2):1512–25.
[33] Mohanraj V, Chen Y. Nanoparticles-a review. Trop J Pharm Res 2006;5 (1):561–73.
[34] Ayinla RT, Dennis J, Zaid H, Sanusi Y, Usman F, Adebayo L. A review of technical advances of recent palm bio-waste conversion to activated carbon for energy storage. J Clean Prod 2019;229:1427–42.
[35] Ruys AJ. Metal-reinforced ceramics. Woodhead Publishing; 2020.
[36] Chakraborty AK. Mullite Formations: Analysis and Applications. Jenny Stanford Publishing; 2021.
[37] Jang JM, Lee W, Ko S-H, Han C, Choi H. Oxide formation in metal injection molding of 316L stainless steel. Arch Metall Mater 2015;60(2B):1281–5.
[38] Cheng X, Feng Z, Li C, Dong C, Li X. Investigation of oxide film formation on 316L stainless steel in high-temperature aqueous environments. Electrochim Acta 2011;56(17):5860–5.
[39] Deng X et al. Microstructure and mechanical performance of porous mullite ceramics added with TiO2. Ceram Int 2020;46(6):8438–43.
[40] Paiman SH, Rahman MA, Othman MHD, Ismail A, Jaafar J, Abd Aziz A. Morphological study of yttria-stabilized zirconia hollow fibre membrane prepared using phase inversion/sintering technique. Ceram Int 2015;41 (10):12543–53.
[41] Hubadillah SK, Othman MHD, Ismail A, Rahman MA, Jaafar J. The feasibility of kaolin as main material for low cost porous ceramic hollow fibre membrane prepared using combined phase inversion and sintering technique. Jurnal Teknologi 2017;79(1–2):pp.

[42] dan Sinteran F. A fabrication of a low–cost zeolite based ceramic membrane via phase inversion and sintering technique. Malaysian J Anal Sci 21(2) 391-401, 2017.

[43] Gupta K, Gupta N. Advanced electrical and electronics materials: processes and applications. John Wiley & Sons; 2015.

[44] Yanu CA, Sieliechi JM, Ngassoum MB. Optimization of ceramic paste viscosity use for the elaboration of tubular membrane support by extrusion and its application. J Mater Sci Chem Eng 2020;8(03):1.

[45] Kingsbury BF, Li K. A morphological study of ceramic hollow fibre membranes. J Membr Sci 2009;328(1–2):134–40.

[46] Wang B, Lai Z. Finger-like voids induced by viscous fingering during phase inversion of alumina/PES/NMP suspensions. J Membr Sci 2012;405:275–83.

[47] Greenberg A, Khare V, Zartman J, Krantz W, Todd P. Macrovoid defect growth during evaporative casting of polymeric membranes. In: 2002 Microgravity Materials Science Conference; 2003.

[48] Chong JY, Wang B, Li K. High performance stainless steel-ceramic composite hollow fibres for microfiltration. J Membr Sci 2017;541:425–33.

[49] Zhu L, Chen M, Dong Y, Tang CY, Huang A, Li L. A low-cost mullite-titania composite ceramic hollow fiber microfiltration membrane for highly efficient separation of oil-in-water emulsion. Water Res 2016;90:277–85.

[50] Fung Y-L-E, Wang H. Investigation of reinforcement of porous alumina by nickel aluminate spinel for its use as ceramic membrane. J Membr Sci 2013;444:252–8.

[51] Mohtor NH, Othman MHD, Ismail AF, Rahman MA, Jaafar J, Hashim NA. Investigation on the effect of sintering temperature on kaolin hollow fibre membrane for dye filtration. Environ Sci Pollut Res 2017;24(19):15905–17.

[52] Bonyadi S, Chung T-S, Krantz WB. Investigation of corrugation phenomenon in the inner contour of hollow fibers during the nonsolvent-induced phase-separation process. In: Hollow Fiber. Membranes: Elsevier; 2021. p. 85–104.

[53] Balcázar-Arciniega C, Hernández-Olivares F. Assessment of the relationship between diameter and tensile strength of piassaba (aphandra natalia) fibers.

In: Sustainable Development and Renovation in Architecture, Urbanism and Engineering: Springer; 2017. p. 227-237.

[54] Jiang Y, Liu X, Gao H, He Y. Reactively synthesized porous Ti3SiC2 compound and its mechanical properties with different apertures. Crystals 2020;10(2):82.

[55] Korminouri F, Rahbari-Sisakht M, Rana D, Matsuura T, Ismail A. Study on the effect of air–gap length on properties and performance of surface modified PVDF hollow fiber membrane contactor for carbon dioxide absorption. Sep Purif Technol 2014;132:601–9.

[56] Fung Y-L-E, Wang H. Nickel aluminate spinel reinforced ceramic hollow fibre membrane. J Membr Sci 2014;450:418–24.

[57] Dewi R, Agusnar H, Alfian Z. Characterization of technical kaolin using XRF, SEM, XRD, FTIR and its potentials as industrial raw materials. J Phys: Conf Ser 2018;1116(4). IOP Publishing, p. 042010.

[58] Das C, Bose S. Advanced ceramic membranes and applications. CRC Press; 2017.

[59] Song C, Wang T, Pan Y, Qiu J. Preparation of coal-based microfiltration carbon membrane and application in oily wastewater treatment. Sep Purif Technol 2006;51(1):80–4.

[60] Al-Alawy AF, Al–Musawi SM. Microfiltration membranes for separating oil/water emulsion. Iraqi J Chem Petrol Eng 2013;14(4):53-70.

[61] Vickers NJ. Animal communication: when i'm calling you, will you answer too? Curr Biol 2017;27(14):R713–5.

[62] Hubadillah SK, Othman MHD, Rahman MA, Ismail A, Jaafar J. Preparation and characterization of inexpensive kaolin hollow fibre membrane (KHFM) prepared using phase inversion/sintering technique for the efficient separation of real oily wastewater. Arab J Chem 2020;13(1):2349–67.

[63] Liu M, Zhu Z, Zhang Z, Chu Y, Yuan B, Wei Z. Development of highly porous mullite whisker ceramic membranes for oil-in-water separation and resource utilization of coal gangue. Sep Purif Technol 2020;237:116483.